Machine learning accelerated photodynamics simulations

Jingbai Li[a]* and Steven A. Lopez[b]*

[a]Hoffmann Institute of Advanced Materials, Shenzhen Polytechnic, 7098 Liuxian Boulevard, Shenzhen, Guangdong 518055, P. R. China
[b]Department of Chemistry and Chemical Biology, Northeastern University, Boston, MA 02115, USA

*Correspondence to lijingbai@szpt.edu.cn and s.lopez@northeastern.edu

Abstract
Machine learning (ML) continues to revolutionize computational chemistry by accelerating predictions and simulations by training on experimental or accurate but expensive quantum chemical (QC) calculations. Photodynamics simulations require hundreds of trajectories coupled with multiconfigurational QC calculations of energies, forces, and non-adiabatic couplings that contribute to the prohibitive computational cost at long timescales and complex organic molecules. ML accelerates photodynamics simulations by combining nonadiabatic photodynamics simulations with an ML model trained with high-fidelity QC calculations of energies, forces, and non-adiabatic couplings. This approach has provided time-dependent molecular structural information for understanding photochemical reaction mechanisms of organic reactions *in vacuum* and complex environments (i.e., explicit solvation). This review focuses on the fundamentals of QC calculations and machine learning techniques. We then discuss the strategies to balance adequate training data and the computational cost of generating these training data. Finally, we demonstrate the power of applying these ML-photodynamics simulations to understand the origin of reactivities and selectivities of organic photochemical reactions, such as *cis-trans* isomerization, [2+2]-cycloaddition, 4π-electrostatic ring-closing, and hydrogen roaming mechanism.

1. Introduction

Photochemical reactions are ubiquitous and responsible for many processes, including photosynthesis, vision, photocatalysis, and photodissociation. They generally occur in mild conditions with high atomic economies and provide synthetic tools with excellent spatiotemporal control over chemoselectivity, regioselectivity, and stereoselectivity. These essential features enable building molecular frameworks from designed molecules[1-3] to structurally complex natural products.[4-6] As such, photochemical reactions are gaining increasing importance in academic research and industrial applications for the synthesis of energy-dense fuels,[7-11] innovation of energy storage devices,[12-16] advancement of drug design,[17, 18] and development of novel materials.[19, 20]

Photochemical reactions begin with a ground-state molecule absorbing a photon with an appropriate frequency to promote an instantaneous electronic transition to an excited state of the same spin multiplicity. The subsequent processes redistribute the absorbed energy along the molecular vibration modes on the excited-state potential energy surface (PES), which leads to structural transformations. In contrast to light-induced luminescence as the consequence of the radiative decay, photochemical reaction undergoes a nonradiative decay relaxing the photoexcited molecule to the ground state as a product or ground-state reactive intermediate. Recent developments in time-resolved spectroscopic technologies allow chemists to study photochemical reactions on an ultrafast timescale.[21-23] In principle, the instrument, for instance, transient absorption spectroscopy, can probe the excited-state dynamics of photoexcited molecules and provides structural information. At the same time, the reacting species evolve during photochemical reactions. However, interpreting the molecular vibrations becomes increasingly complicated for conformationally flexible molecules with competing non-radiative mechanistic pathways. The increasing degrees of freedom lead to elusive spectroscopic data, where the excited-state vibrational modes involve multiple synchronous bond stretching or

torsions. Moreover, the timescale resolution of spectroscopy techniques (i.e., transient absorption and time-of-flight mass spectroscopy) is infeasible to capture all transient intermediates and molecules in excited states.
Quantum mechanics provides a theoretical framework to understand the relationship between molecular excited-state structures and their reactivities and selectivities. Calculations of the electronic transitions and the mechanistic critical points along the relevant excited-state PES provide unprecedented knowledge of the time-dependent evolution of molecular excited states toward photoproducts.

The theories derived from a static PES in equilibrium often fail to explain the reaction mechanisms of the photochemical reactions over a vast range of timescales (10^{-15} to 10^{-3} s). As such, dynamical effects must be considered to understand experimental quantum yields or predict the outcome of unknown photochemical reactions. These dynamical effects can be simulated with nonadiabatic molecular dynamics (NAMD). The mixed quantum-classic (MQC) trajectory formalism of NAMD is widely used to capture the dynamical effects on the excited- and ground states on-the-fly. The MQC trajectory propagates along an excited-state PES using classical mechanics by solving Newton's Equation of Motion. Quantum chemical methods evaluate nuclear forces by solving approximations to Schrödinger's Equation. Despite the flexibility and accuracy of NAMD simulations, they can have a prohibitive computational cost because they rely on thousands of consecutive QC calculations along a reaction coordinate. Thus, the NAMD simulation based on time-dependent density functional theory (TDDFT) and post-Hartree-Fock (HF) calculations are commonly limited to medium-sized molecules with 40–50 atoms and timescales of only a few picoseconds.[24, 25] Therefore, many research groups are developing new approaches to extend the length and timescale of NAMD, such as improving the accuracy of semiempirical methods,[26-28] fitting analytical potential with linear vibronic coupling model[29, 30] and accelerating QC calculations with GPU.[31]
With the rise of high-performance computing resources, researchers worldwide have generated massive amounts of data; ML has been used to design molecules that intelligently satisfy multiple properties.[32, 33] Examples of these include material design and drug discovery,[34, 35] reaction barrier prediction,[36] transition states search,[37-39] solving the Schrödinger equation[40, 41] modeling wave functions,[42, 43] optimizing density functionals,[44, 45] and predicting IR,[46] UV-Vis,[47, 48] and NMR[49] spectra. The main advantage of ML is that it can effectively learn the *N*-dimensional relationships of any input-output relation datasets that are otherwise overwhelming to humans. This feature enables the development of ML potential as an alternative for QC calculations to predict excited-state PESs for NAMD at a negligible computational cost without losing accuracy.

This review provides an overview of recent developments in ML photodynamics. We will first discuss the fundamentals of the theoretical methods integrated into the ML photodynamics approach, including the QC methods available for generating accurate reference data of excited-state electronic properties. Then we will review the NAMD approaches compatible with ML potentials for simulating photochemical reactions, the ML techniques ready for fitting excited-state PESs with QC reference data, and the training data generation strategies. Then, the following sections will summarize the applications of ML photodynamics with recent studies on photochemical reaction mechanisms, such as *cis-trans* isomerization, [2+2]-cycloadditions, 4π-electrocyclic ring-closing reactions, and hydrogen roaming. Finally, the discussions will be focused on the emerging chemical problems in photochemical reaction research and the technical details of the employed QC and ML methods.

2. Methods

We first introduce the methods used in the ML photodynamics simulation. Figure 1 illustrates a brief flowchart for choosing appropriate methods in our experience, explained by the following discussions.

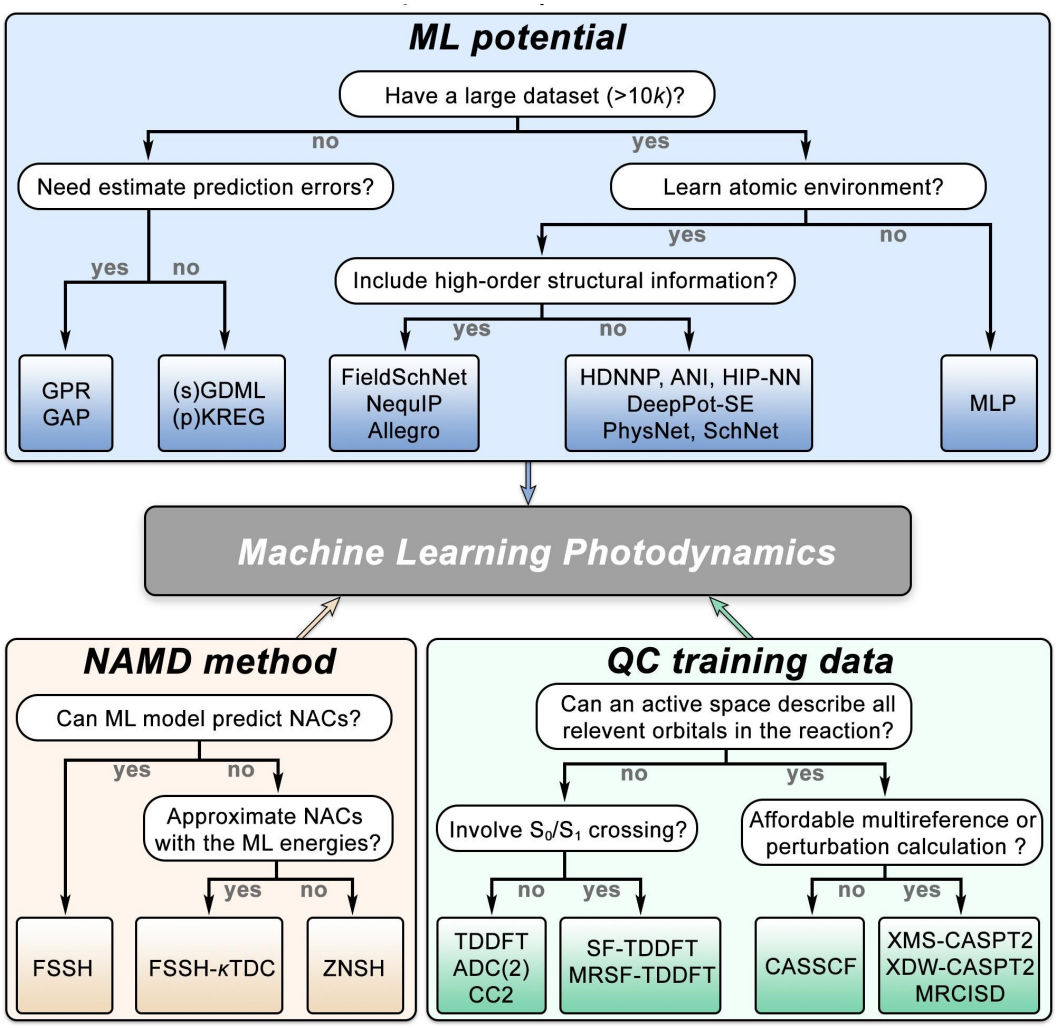

Figure 1. Flowchart for choosing machine learning models, nonadiabatic dynamics methods, and quantum chemical methods for training data calculations.

2.1. *Machine learning methods*

ML methods are popular for developing fast and accurate potential models for molecular dynamics simulations.[50, 51] For photodynamics simulations, the ML potential learns the relationships between the molecular structures and the ground and excited-state electronic properties, for instance, energies, forces, nonadiabatic couplings (NACs), and spin-orbit couplings (SOCs). The molecular descriptor numerical representation encodes three-dimensional structural information. The ML model reads the molecular descriptor to predict the ground and excited-state energies, forces, NACs, and SOCs by minimizing the errors between the expected numbers and the ground-truth data. Selection of the ML models and molecular descriptors needs extraordinary carefulness because they are two main factors determining the accuracy of the ML potentials for photodynamics simulations.

Kernel and neural networks (NNs) are popular methods for training ML potentials (Figure 1). The kernel methods (*e.g.*, Kernel ridge regression and Gaussian process regression) are nonparametric to search the form of the kernel functional depending on the training data that make probabilistic predictions. The complexity and number of parameters of kernel methods increase as the training data expands. Neural networks optimize a fixed number of predefined hidden layers and node parameters by minimizing a loss function (*e.g.*, mean square error). This NN architecture is called a multiple-layer perceptron (MLP). The optimization of NN also requires tuning hyperparameters (e.g., activation functions, number of hidden layers and nodes, learning rates, and regularizations). Since the complexity of the NN is independent of the training data, it is expected to have good computational scaling and memory usage for

large training sets, including photodynamics simulations. Various ML potentials have been developed to improve the accuracy of the predicted potential energies and forces, such as high-dimensional neural network potential (HDNNP),[52] SchNet,[53] PhysNet,[54] ANI,[55, 56] deep potential smooth edition (DeepPot-SE),[57] symmetrized gradient-domain machine learning (sGDML),[58] permutationally invariant kernel ridge regression using RE descriptor and the Gaussian kernel (pKREG),[59] reproducing kernel Hilbert space (RKHS),[60] Gaussian approximation potential (GAP),[61] neural equivariant interatomic potential (NequIP),[62] and local equivariant deep neural network interatomic potential (Allegro).[63] Some packages of a collection of ML methods are MLatom,[59, 64] and fast learning of atomic rare events (FLARE).[65] A comparison of NN and kernel methods show similar accuracies for ML photodynamics simulations.[66] More benchmarks on various ML potentials are reviewed in these references.[50, 67, 68]

Molecular descriptors must satisfy the translational and rotational invariance to hold a valid and machine-learnable mapping between molecular structures and corresponding energies and forces. These requirements motivate the development of global descriptors such as internal coordinates, Coulomb Matrix,[69] and inverse distance matrix.[70] The global descriptors above are not invariant with respect to the permutation of chemically equivalent atoms. Permutation-invariant representations are created with sorting techniques (e.g., bag-of-bonds,[71] and randomly sorted Coulomb matrices[72]). However, it could result in discontinuous PESs, where the ML potential becomes challenging to train. Permutationally invariant polynomials[73] is another solution applicable only for small molecules as the number of permutations grows exponentially with molecular complexity. We have introduced the permutation map technique[74, 75] to restore the permutationally invariant structural information from existing training data according to molecular symmetry. Alternatively, we can choose a local descriptor representing the local chemical environment around each atom with a set of basis functions in a given cutoff sphere. The local descriptors are permutationally invariant and size extensive because they decompose the total energy into atomic contributions. Some examples of local descriptors are atom-centered symmetry functions (ACSFs),[76] smooth overlap of atomic positions (SOAP),[77] and Faber−Christensen−Huang−Lilienfeld (FCHL).[78] Pozdnyakov and co-workers addressed the significance of the higher-order terms in the local descriptors.[79] The high-order terms improve the atomic structure representations by adding angular information beside the interatomic-distanced-based radial information. Using physics-informed descriptors can achieve high-accuracy ML performance with minimal training data.

Recent NN-based ML potentials incorporate the local descriptor in the model, thus enabling simultaneous optimization of the descriptors and model parameters during the training. Message-passing neural networks (MPNN) implement such descriptors.[80] MPNNs embed the atomic information (e.g., atom type) using discrete numbers, called node features, and the interatomic information using a transformation function of the pairwise atomic distances, called edge features. The node and edge features go through the message-passing layer that updates the node features by convoluting the neighboring node features weighted by the corresponding edge features within a local environment following the molecular connectivity graph. Iterative updating of node features with a message-passing layer refines the encoded messages on each atomic center. Their sum is used to fit the molecular properties (*e.g.*, total energy). Increasingly sophisticated convolutional layers are introduced to extract the atomic features acting as a pattern filter for the local atomic environment. This type of convolutional layer was implemented in Deep Tensor NN (DTNN)[53] and the descendant SchNet,[81] which uses Gaussian functions to learn the internuclear distance for fitting molecular potential and force field. Similar NNs are PhysNet, [54] HIP-NN,[82] DeepPot-SE,[57] SchNOrb,[42] and SpookyNet.[83] The Gaussian functions only transform the node and edge features as scalers, which is inefficient for learning the angular information. Spherical harmonic functions allow NN to learn the node and edge features in the form of tensors. These geometrical tensors can represent the radial, angular, and high-order structural information, significantly accelerating

the training with a minimum amount of data. The convolution of tensors requires special tensor product operations satisfying the translational and rotational invariance, which is implemented in Euclidean equivariant neural networks (e3nn).[62] NequIP[62] and Allegro[63] are two applications of e3nn for learning the atomic potential. NequIP outperforms existing ML models with high accuracy but up to three orders of magnitude fewer data sets;[62] and the Allegro, with similar accuracy to NequIP, achieves high learning and prediction efficiency in simulating a system with 100 million atoms.[63] To the best of our knowledge, many graph convolutional NNs (GCNN) are available for ground-state molecular dynamics, but only a few have been adapted for photodynamics simulations.

Researchers can learn excited-state PESs based on a time series of molecular geometries in NAMD trajectories with recurrent NNs (RNNs).[84] The RNN uses a directional connective graph that passes the outputs of the previous step as inputs of the current step. It predicts further data by considering the historical evolution's memory information, which extracts the temporal features. The long short-term memory (LSTM) units are used to avoid gradient vanishing and exploding problems.[85] Recent work by Gu and Lan has reported successful multi-configuration time-dependent Hartree (MCTDH) dynamics simulations using LSTM-NN.[86] Due to the complexity of input data constructions-a time series of geometries rather than a single geometry, the LSTM-NN has not been used for simulating photochemical reactions. Nevertheless, the LSTM-NN shows a promising solution to avoid problems in learning NAC. The NACs are essential in the FSSH method because it determines the time evolution of the state population, which controls the surface hopping probability. A recent work by Shen and co-workers showed that LSTM-NN could learn the state population in a given number of consecutive snapshots in trajectories.[84] As such, the NACs are no longer needed as the predicted state population matrix can be directly used to compute the surface hopping probability for FSSH. Although this approach successfully worked for analytical models, applications in molecular systems have yet to be reported.

2.2. *Nonadiabatic molecular dynamics*

The ML photodynamics stems from the NAMD methods using MQC trajectories. Nuclear motions are treated classically along a single PES. Omitting nuclear quantum effects substantially accelerates these simulations and enables the simulation of full-dimensional NAMD photodynamics of interesting, practical molecules. [24, 25] The most time-consuming step is the computation of ground- and excited-state energies and forces because the MQC trajectory requires sequential on-the-fly computations at each timestep. Furthermore, a typical NAMD simulates an ensemble of independent MQC trajectories to obtain statistically meaningful results. As such, the number of trajectories multiplied by the number of nuclear geometries gives thousands of QC calculations resulting in a prohibitive computational cost.

In the NAMD simulations with MQC trajectories, the trajectory propagates along an electronic state of a PES. The surface hopping algorithm describes the nonadiabatic electronic transition(s) by hopping between the electronic states in degeneracy regions with strong NACs, known as trajectory surface hopping (TSH). Fewest switches surface hopping (FSSH) is a widely used algorithm to determine the probability of surface hopping. It requires information on the nonadiabatic couplings (NACs) between the PESs with the same spin multiplicity and the spin-orbit couplings (SOCs) between PESs with different spin multiplicities, e.g., singlet and triplet.[87, 88] Many photochemical reactions have been studied using the FSSH dynamics method.[89-91] However, learning NACs for ML photodynamics is challenging for the following reasons. 1) The number of NACs increases with the number of PESs quickly in a relationship of $N \cdot (N - 1)/2$ for an N-state system. Since modeling photochemical reactions involves at least two states, the computations of NACs become the most expensive part of generating the QC training dataset. 2) The NACs are in an arbitrary phase because the wave functions of two electronic states are usually randomly initialized. NAMD simulation commonly performed phase corrections based on the overlap of NACs over two continuous timesteps. However, the training data does not enforce structural continuity. There is no guarantee that the structures

are in the same order as them in the trajectory or the same trajectory. The phase corrections are performed with additional geometrical interpolative techniques.[92] On the other hand, a phaseless loss function was introduced to train NNs regardless of the phase of NACs data.[92] For each state pair, the NAC data are multiplied by the phase factor (i.e., +1 or –1) to evaluate the prediction errors. The combination of phase factors with the lowest fitting error corresponds to the phase-corrected NAC data and will be used to train the NNs. The main drawback of this approach is that the loss function calculations scale with 2^{N-1} for N states. It becomes inefficient when N is large. For instance, fitting the NACs over five states would evaluate the loss function 16 times. 3) NACs, defined in Eq. 1, are sensitive to the inverse of the energy gaps between the two coupling states. It is nearly zero for almost all points along a photodynamics simulation except for near avoided crossings or conical intersections. The magnitude suddenly approaches infinity as the molecule approaches the state-crossing. The discontinuous NAC function leads to a highly challenging ML task that still does not have a general solution. A remedy to this issue is learning the numerator terms of the NACs, which is a continuous function of reaction coordinates avoiding cusp data.[92] Then, the full NACs can be computed on-the-fly by dividing the gaps between the ML-predicted energies. Still, the above approach remains difficult to predict the NACs at the degeneracy regions, where the ground-truth energy gap could be smaller than the prediction error within the so-called chemical accuracy of 1.0 kcal mol^{-1}. Nevertheless, this approach has successfully predicted several molecules' excited-state dynamics and photochemical reactions.[92, 93] 4)The NACs are vectorial properties as they indicate the steep descent directions for the changes of two coupled wave functions. They must be learned together with the geometries satisfying the translation invariance and rotational covariance. Marquetand and co-workers constructed a virtual ML potential and used the first-order derivatives to fit the numerator term of the NAC data.[92] In contrast to the straightforward physical relationship between energy and force, the physical meaning of the virtual potential is unclear. Thus, the training data are unavailable to improve the accuracy of the virtual potential. It worked for model systems (e.g., $CH_2NH_2^+$), but we have seen overfitting issues in molecules beyond these systems.[74, 94, 95]

$$d = \left\langle \psi_i \left| \frac{\partial H}{\partial R} \right| \psi_j \right\rangle \frac{1}{E_i - E_j} \quad (Eq.\,1)$$

An alternative to learning NACs is Zhu-Nakamura's theory of surface hopping (ZNSH).[96, 97] The ZNSH method uses a generalized one-dimensional model to describe the nonadiabatic transition, where the forces are diabatized based on three-point interpolation. It computes the surface hopping probability based on an analytical equation of energy gap and forces, which is generalizable to include SOCs for intersystem crossing mechanisms.[98] The ZNSH method requires the forces of all involved states instead of the current state in FSSH, leading to relatively expensive QC calculations. Fortunately, the ML forces and energies are learned simultaneously. As such, the ZNSH method can take full advantage of the ML acceleration in ML photodynamics simulations. The ZNSH method has shown comparable results to the FSSH method for studying several molecules' excited-state dynamics and photochemical reactions.[97, 99, 100]

Another solution to the NAC problem relies on on-the-fly computed NACs with the Baeck-An (BA) approximation;[101, 102] the BA approximation computes NACs as a function of the second-order derivative of the energy gap with respect to the nuclear positions. While calculating the second-order derivative of the energy gap is time-consuming, the auto differentiation techniques are compatible with ML techniques due to the analytical evaluations of second-order derivatives. By transferring the energy gap derivatives from the geometric domain to the time domain, we can numerically compute the second-order derivative by evaluating the temporal changes of energy gaps along with three adjacent time steps.[103] The approximated NACs are also termed curvature-approximated time derivative couplings (κTDC), as their quantities only depend on the curvature of PES.[103] The κTDC approach enables ML FSSH photodynamics, which is notably less empirical than ZNSH dynamics. Figure 1 demonstrates

that the NAMD method choice for ML photodynamics simulations depends on the rigor of the available NAC computations.

2.3. *Quantum chemical methods*

Choosing an appropriate QC method for excited-state calculations is essential to prepare accurate training data for ML photodynamics simulations (Figure 1). Single and multireference methods are two common types of QC methods popular for studying electronic properties and nuclear dynamics in excited states. Single-reference (SR) methods compute excited-state electronic structures using the ground state as a reference under the adiabatic approximation, such as time-dependent density functional theory (TDDFT),[104] approximate second-order coupled-cluster (CC2),[105] and algebraic diagrammatic construction to the second order (ADC(2)).[106, 107] However, SR methods suffer some deficiencies in studying excited states in the following cases. 1). The SR method based on single excitations, e.g., TDDFT, cannot describe the double excitation. 2). The SR methods do not treat the ground and excited-state wavefunction on equal footing; thus cannot correctly compute the excited states degenerate to the ground state. These situations are often encountered in computing photochemical reaction pathways, where the doubly excited state could participate in the reaction, and the reactions could go through regions of degeneracy between the ground and excited state (e.g., avoided crossings and conical intersections). Moreover, the SR methods produce the wrong dimensionality for the branching plane of singlet conical intersections because the single excitation formulation computes incorrect interaction between the ground and excited states. This issue results in a problematic energy relaxation path from a conical intersection.[108, 109] Spin-flip technique (e.g., SF-TDDFT)[110, 111] was introduced to restore correct PESs surrounding conical intersections. Other methods, such as the mixed reference spin-flip TDDFT (MRSF-TDDFT)[112] and spin-restricted ensemble-referenced Kohn–Sham (REKS)[113] can compute conical intersection at the cost of SR methods.

Multiconfigurational methods are sufficiently robust to describe conical intersections' electronic structures and nuclear geometries. Many works have shown that the conical intersections computed by multiconfigurational methods are required to explain the mechanism and obtain the structure-reactivity relationships in photochemical reactions.[89-91] The multiconfigurational methods often use reference wave function generated by the complete active space self-consistent field (CASSCF). The CASSCF wavefunction includes the full configurational interactions in a subset of molecular orbitals, called active space, that can fully address issues in the abovementioned single-reference method. Two popular multiconfigurational methods are complete active space second-order perturbation theory (CASPT2)[114, 115] and multireference configuration interaction (MRCI).[116-119] CASPT2 directly adds second-order perturbative corrections (i.e., dynamical correlation) to the CASSCF excited-state energies; MRCI computes the electronic excitations by generating single and double electron transitions on top of the CASSCF wavefunctions. Moreover, the extended multistate (XMS)[120] and dynamically weighted (XDW)[121] variants of CASPT2 improve the energy corrections near the state-crossing regions. It is important to remember that the MR methods rooted in CASSCF have limitations. 1). modern QC software limits the active space size to 22 electrons and 22 orbitals due to the exponential growth of the configuration state functions. Recent developments in the adaptive sampling configuration interaction (ASCI) method have expanded the active space size beyond 50 electrons and 50 orbitals.[122, 123] 2) The active space and the state-averaging choice are not trivial. In our experience, the results depend on the researcher's expertise with multiconfigurational methods and active space selection prowess. 3) MR calculations are significantly more expensive than SR calculations because they need to optimize the configuration and orbital coefficients simultaneously or asynchronously. They are only affordable to study the excited states of small molecules.[90, 124, 125] CASSCF is more frequently used for medium-sized molecules,[91, 126] although the lack of dynamical correlation often overestimates the excitation energies.[127] As such, the CASSCF results must be validated against the multireference calculations to confirm the consistent electronic nature (i.e.,

topology) of the excited-stated PESs along the photochemical reaction pathway. Neither single nor multireference methods may be available to describe the entire photochemical reaction pathways, where a combination of QC methods can be employed.[128, 129]

2.4. *Training data*

The performance of ML potential in predicting photochemical reactions highly relies on the quality of training data. The training data for photodynamics simulations requires sufficiently sampling the structures on the ground and excited-state PESs (*i.e.*, configurational space). This task requires different types of training data from the commonly used molecular structure and properties database across the chemical compound space, such as QM7,[130] QM7b,[131] QM8,[132] and QM9.[133] The MD17 database, for instance, is popular for benchmarking ML potential across ground-state configurational space for small organic molecules.[134] A more recent WS22 database provides 1.18 million equilibrium and non-equilibrium geometries of molecules up to 22 atoms, sampled from Wigner distributions centered at different ground-state conformations.[135] The design of the WS22 database has been quite helpful for benchmarking ML potential for excited-state dynamics. The diversity in chemical composition and accessible conformations assures a broad and statistically robust representation of the PESs.

Photodynamics simulations could lead to an immense amount of excited-state molecular geometries outside the existing databases. Unfortunately, a universal ML potential trained with existing data for the excited states of the molecules with various sizes and compositions is not available. The main reason is that the excited-state energy is an intensive quantity that cannot decompose into atomic contributions. Second, the excited-state electronic energy is not a smooth function of nuclear configurations, especially near the state-crossing region, if the number of computed excited states is insufficient. However, it is impossible to determine the number of excited states for all molecules and photochemical reactions. Molecules can go through various states in photochemical reactions depending on the nature of absorption and wavelength of the employed light source. Therefore, training ML potentials for photodynamics simulations requires generating tailored training data for a specific photochemical reaction.

There are two main strategies for training data generation, human-designed and data-driven approaches. The human-designed approach is based on well-designed molecular structure sampling methods, such as the MD-based methods (umbrella sampling,[136] trajectory-guided sampling,[137] enhanced sampling,[138] and metadynamics[139]), stochastic surface walk,[140] Wigner sampling,[141] and normal mode scans.[92, 142] These methods have been applied for learning thermal reactions; however, the data sampling efficacy is limited for complex photochemical reactions. For instance, ground-state MD simulations access different mechanistic pathways from excited-state processes, while excited-state MD becomes prohibitively expensive as the number of degrees of freedom increases. Wigner sampling for the reactant or product geometries captures only accessible nonequilibrium geometries near local or global minima. Normal mode scans include many irrelevant molecular vibrations. A composite scheme that combines Wigner sampling and geometrical interpolation could overcome the individual limitation to generate a compact yet relevant initial set.[94] A similar approach has been used to generate the WS22 database.[135] The data-driven approach, also called adaptive sampling (Figure 2) or active learning, is more efficient and nearly eliminates human bias. The objective is to train an initial ML potential with available computed training data and use it to explore the excited-state PESs with the active learning algorithm. The simulations monitor the ML predictions with a measure of uncertainty in the predicted values to determine the undersampled data. The uncertain data are recomputed with multiconfigurational QC calculations to expand the original training dataset, iteratively improving the ML potential by retraining the model with new data until no undersampled data is found. The uncertainty metric is available in the kernel methods such as Gaussian Process Regression (GPR), as it always returns the prediction's covariance. However, a single NN model does not have an uncertainty

measure. Our group has followed the concept of the *query by committee*,[143] where two NNs are independently trained, and the standard deviation between their predictions quantifies the uncertainty.

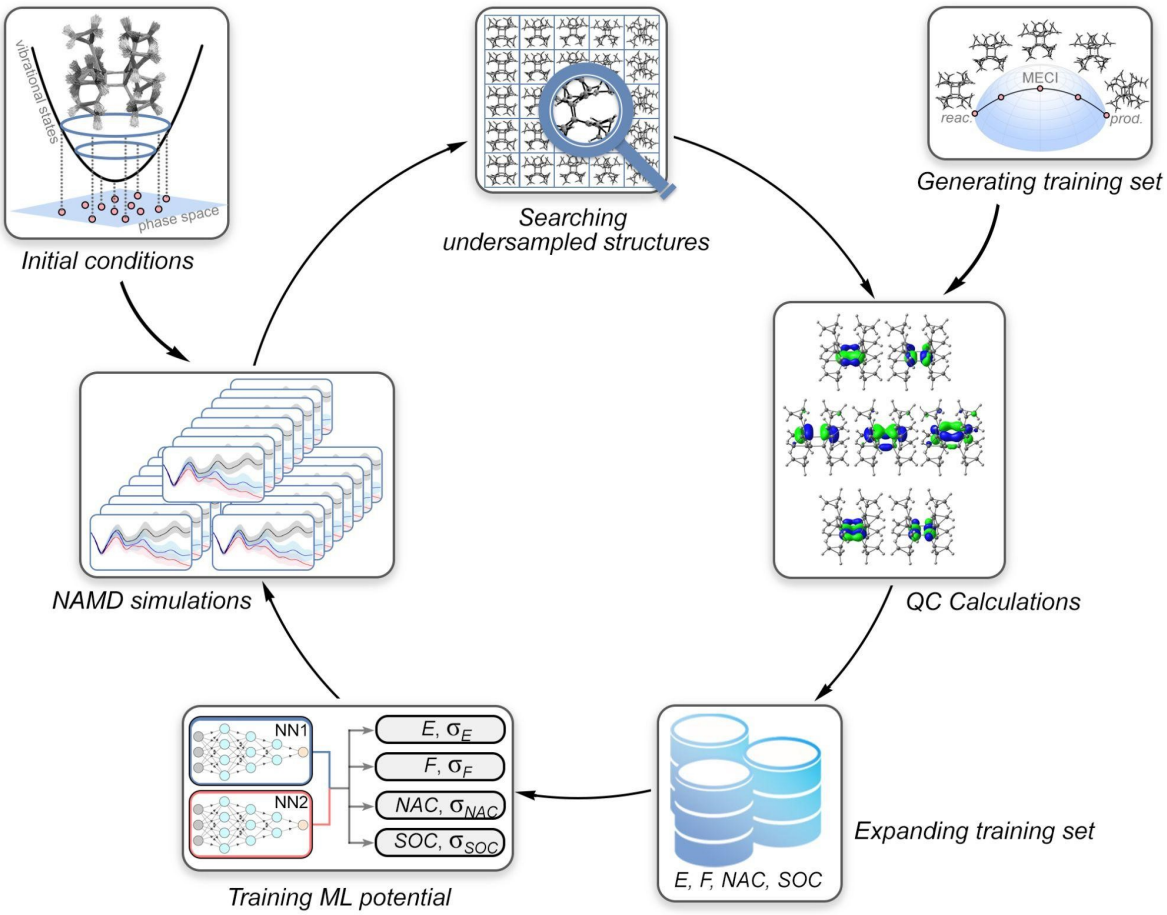

Figure 2. Schematic demonstration for the adaptive sampling procedures. The workflow starts by generating a training set with Wigner sampling and geometrical interpolations. The QC calculations produce the initial data to train two NNs. The initial conditions of NAMD simulations reuse the Wigner sampled structures; the NNs predict energies, gradients, NACs, and SOCs to propagate surface hopping trajectories. If the prediction standard deviations (σ) of NNs are large, the energies, gradients, NACs, and SOCs of the current structure are recomputed and added to the training data. Then NNs are retrained to restart NAMD simulations. If the prediction standard deviations are sufficiently small, the training cycle completes.

The advantage of adaptive sampling is that the training process automatically explores the excited-state PESs, searching all possible photochemical reaction pathways. It benefits the training data preparation as it requires knowledge of one of the possible competing photochemical reactions. The recent study on the photochemical [2+2]-cycloaddition of [3]-ladderdiene toward cubane has shown the efficiency of adaptive sampling, discovering the unseen structures and reactions mechanism based on exclusive information about the [2+2]-cycloaddition pathway.[74]

2.5. *Multiscale approaches with ML potential*

Photochemical reactions of interest to organic chemists rarely occur in the gas phase; solvated media are much more common. Capturing chromophore-solvent interactions and understanding their role using QC methods is challenging because of the exponential scaling with the system size. Multiscale approaches divide the complex environment of chromophore and surroundings into at least two components. The chromophore undergoing the

photochemical reaction is typically treated with a quantum mechanical (QM) method to account for bond breaking and forming. In contrast, the surrounding explicit solvent molecules are treated with a lower level of theory (e.g., classical force field or semiempirical method). These simulations are known as QM/MM when the solvated chromophore is treated with a QM method and the surrounding solvent molecules are treated with a classical force field.[144] The computational cost of this simulation can still be prohibitively high when the QM method is multiconfigurational (i.e., CASSCF), thus integrating an ML potential into multiscale approaches enables the ML/MM, ML/semi-empirical (QM'), or QM/ML methods with higher efficiency and applicability than the QM/MM methods.

Herein, we briefly introduce the QM/MM methods to show how ML potential can be adapted into multiscale approaches. Different flavors in the QM/MM methods have been implemented to compute the center chromophore's energy and the whole system's total energy with the environment. The total energy of the chromophore and environment can be evaluated in a subtractive and additive scheme. The MM energy of the chromophore is replaced by the QM energy to remove the double-counted MM contributions in the MM total energy in the subtractive scheme. The nonbonded interactions between the chromophore and the environment, including electrostatic and Van der Waals interactions, are computed at the MM level. Alternatively, the total energy is obtained by summing up the QM energy of the chromophore, the MM energy of the environment, and the QM/MM coupling term accounting for the nonbonded interactions.

The ML potential can improve QM and or MM calculations in the QM/MM methods. In the QM/ML scheme, an ML potential trained with QC calculation data could work as the MM backend. It ensures the same accuracy of the QM and ML energies alleviating mismatched accuracies between the QM and MM energies.[145] By treating the MM region as multilayer energy-based fragments, the QM/ML method has successfully simulated the excited-state dynamics of dimethyldiazene in a solvent box of 40 water molecules.[146] In the ML/MM scheme, one can use the ML potential to correct the energies and forces obtained from the low-cost semiempirical QM (e.g., DFTB) calculations (i.e., Δ-learning), matching the results of DFT calculations. The Δ-learning approach has been reported to accelerate the MD simulations for thermal reactions (e.g., S_{N2} reaction and Claisen rearrangement) using the HDNNP[147-149] and DeepPot-SE.[150] On the other hand, the ML potential, such as HDNNP,[151] FieldSchNet,[152] and Deep-Pot-SE[153] have been adapted to a QM calculator that predicts the energies and forces at the same level as the QM training data. These methods belong to the electronic embedding ML potential. They incorporated additional electronic embedding features to learn the environment-polarized QM data, which properly retains the dependence of energies and forces on the external charges. A similar approach has been implemented to support the electrostatic embedding GPR model.[154] A recent study demonstrated that the embedded atom neural networks (EANN)[155, 156] in a mechanical embedding scheme could be as accurate as the electronic embedding ML potential when choosing an appropriate QM region for training data calculations. The ML/MM methods still have inconsistent energetic descriptions between the QM and MM regions. To mitigate the inconsistency during SchNet model training, a buffered region between the inner QM and outer MM regions was introduced.[157] The buffer region experiences full electronic polarization by the inner QM region. The effective interactions with the QM region are calculated at the QM level, while the interactions with the MM region are described at the MM level. The total interactions are a combination of MM interactions and the effect of the QM region on the electronic degrees of freedom of the buffer region, which minimizes the artifacts arising from mixing QM and MM data.

3. Applications of ML photodynamics for resolving photochemical reaction mechanisms

ML photodynamics has numerous applications for studying excited-state dynamics, nonradiative decay processes, and complex photoreactions. For instance, Maquetant and co-workers demonstrated that both KKR and NN models could learn the excited-state dynamics

of small molecules, such as $CH_2NH_2^+$, $S{=}CH_2$, and SO_2.[66, 93] Haberson and co-workers used the KRR model to perform MCTDC simulations for several molecular systems,[158] explaining the excited-state hydrogen tunneling phenomena.[159] Pavlo and co-workers applied KRR to learn the quantum dissipative dynamics of open systems;[160] they also reported that a CNN model could predict 10-ps-long trajectories of open quantum systems dynamics in one shot.[161] In this section, we will focus on the ML photodynamics application in resolving complex mechanistic questions in photochemical reactions.

3.1. *Photochemical cis-trans isomerization of hexafluoro-2-butene*

The first example demonstrating an automatic discovery of photochemical reaction pathways using ML photodynamics simulations is the NN-predicted *cis-trans* isomerization of hexafluoro-2-butene (Figure 3a).[94] The NN potential was constructed using two independently trained MLP models with the inverse distance matrix representation. The training set was initially generated with the Wigner sampling combined with geometrical interpolations from the *cis* to the *trans*-configuration, complemented with snapshots of short-time (50 fs) NAMD trajectories, which gives a total number of 4961 data points. The training data were computed at CASSCF(2,2)/cc-pVDZ level. Adaptive sampling searched the undersampled geometries. It propagated 250 trajectories from the S_1 state in 500 fs. 80% of the trajectories have finished in 5 iterations finding 565 new geometries. Up to 28 iterations, 98% of the trajectories were completed. It collected an overall of 1516 new geometries leading to a final training set of 6207 data points. The mean absolute errors (MAEs) of energy predictions were 0.023–0.025 eV, satisfying the commonly accepted chemical accuracy of 0.043 eV(1 kcal·mol^{-1}).

The NN predictions of energies, forces, and NACs take 0.01s on a single CPU, which was $3.4 \cdot 10^4$ times faster than the CASSCF(2,2)/cc-pVDZ calculations. The significant accelerations allow us to simulate the dynamics of *trans*-hexafluoro-2-butene up to 10 ns in 50 hours using a single CPU. It also afforded more trajectories than the QC NAMD simulations. For example, the 500 fs simulations of *trans*-hexafluoro-2-butene cost-efficiently propagated more than 5000 trajectories to obtain a statistically sufficient sampling of the photochemical reaction pathways.

Due to the overfitting issue of NACs, the ML photodynamics simulations using FSSH with NN-predicted NACs overestimate the S_1 lifetime of *trans*-hexafluoro-2-butene compared to the reference CASSCF(2,2)/cc-pVDZ trajectories (Figure 3b). The ZNSH with NN-predicted energies and forces could reproduce the QC reference value of 29.0 fs, predicting an S_1 lifetime of 33.5 fs. Given the NN ZNSH trajectories, the final *trans : cis* ratio was 3.5: 1, which is close to the *trans: cis* ratio of 2.8: 1 found in the QC reference trajectories. Characterizations of the trajectories showed that the NN and QC trajectories underwent virtually identical geometrical changes at the S_1/S_0 surface hopping points, showing a similar topology of the S_1/S_0 crossing seam.

In addition to the *cis-trans* isomerization mechanism, photoexcited hexafluoro-2-butene can promote hydrogen migrations forming a carbene intermediate. This pathway was intentionally excluded from the initial training data as human-introduced bias in the underlying photochemical reactions of hexafluoro-2-butene. The adaptive sampling rediscovered the undersample structures corresponding to the hydrogen migration pathways. The final NN trajectories predicted a *trans*: carbene ratio of 1.1: 1, which also agrees with the QC reference value of 1.6: 1. It suggests that ML photodynamics are feasible to study photochemical reactions with minimal prior knowledge of the underlying reactions.

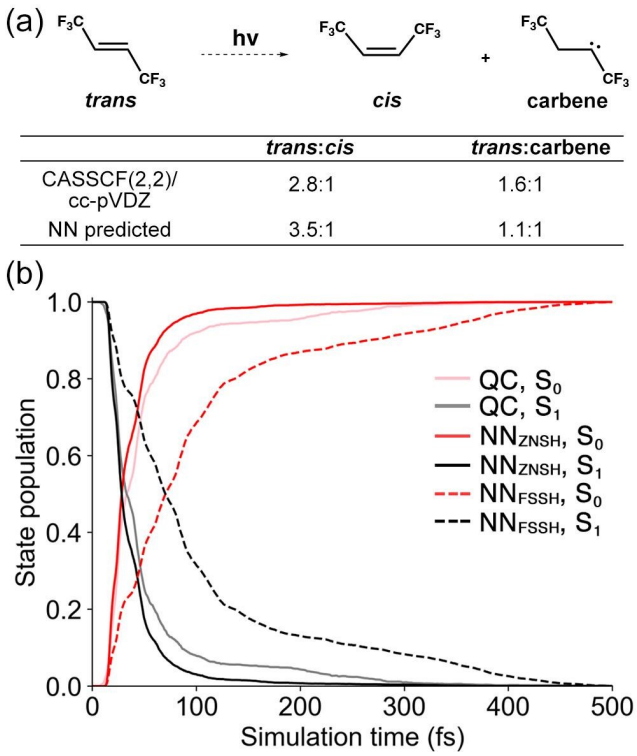

Figure 3. (a) The *cis-trans* isomerization of hexafluoro-2-butene with *trans*: *cis* and *trans*: carbene ratios predicted by 500 fs CASSCF(2,2)/cc-pVDZ and NN trajectories. (b) The state population of hexafluoro-2-butene in 500 fs. QC denotes the FSSH trajectories computed with CASSCF(2,2)/cc-pVDZ calculations. NN_{ZNSH} indicates the NN trajectories with Zhu-Nakamura surface hopping, which does not use NN-predicted NACs. NN_{FSSH} denotes the NN trajectories with FSSH using NN-predicted NACs. The deviation between the QC and NN_{FSSH} trajectories resulted from the overfitted NACs. Results are reproduced from reference[94] with permission from the Royal Society of Chemistry.

3.2. *Photochemical 4π-electrocyclization of norbornyl cyclohexa-1,3-diene*

ML photodynamics simulations can disentangle the photochemistry experiment results beyond the limits of the QC NAMD approach. One such example is the photochemical 4π-electrocyclization of norbornyl cyclohexa-1,3-diene (Figure 4a).[94] The experiment observed a stereoselective ring-closing reaction favoring the *anti*-configuration. Due to the structural complexity and the number of nuclear degrees of freedom, the NAMD simulations with CASSCF(4,3)/ANO-S-VDZP calculations took 17 days to obtain 1 ps dynamics with 240 trajectories. Within the simulation time, two intermediates were predicted, which were not observed in the experiments. The limited number of trajectories also missed predicting the minor product in *endo*-configuration. Thus, the QC NAMD simulations were insufficient to explain the experimental stereoselectivity.

We sought to resolve the mechanism of the 4π-electrocyclization of norbornyl cyclohexa-1,3-diene with the help of the ML photodynamics approach. The NN potential used the MLP model. The training data generations include the Wigner sampling, geometrical interpolation, and sampling from the 50 fs trajectories of QC NAMD simulations. This method generated 3349 training data computed at the CASSCF(4,3)/ANO-S-VDZP level. The adaptive sample further collects the undersampled structures by propagating 250 trajectories in 1 ps. The temperature was increased to 1200 K to accelerate the exploration of high-energy nonequilibrium geometries. During the adaptive sampling, the normal completion of trajectories reached 80% after 6 iterations, then fluctuated in the next 18 iterations. It approached 90% after 50 iterations and stopped at 96% in 100 iterations. The final number of training data is 6272. The MAE of the NN predicted energies are 0.027–0.031 eV.

The ML photodynamics simulations for norbornyl cyclohexa-1,3-diene obtained 3954 trajectories in 1 fs, where a single trajectory only spent 38 s, representing a $3.8 \cdot 10^4$-fold acceleration to the CASSCF(4,3)/ANO-S-VDZP calculation. The increased number of trajectories allows us to observe the less favored pathway toward *endo*-configurations. The predicted yields of the *anti* and *endo*-configuration were 0.7% and 0.2%, respectively. Since the simulations did not include re-excitation of the reformed reactant, the predicted yields are lower than the experimental values of 28% and 4% for the *anti* and *endo*-configuration. Nevertheless, the predicted *anti*: *endo* ratio in the first 200 fs matched the experimental measurements over 4 hours. The ML photodynamics simulations suggested that the *anti*-configuration is favored because its S_1/S_0 crossing regions are more accessible than the *endo*-configuration.

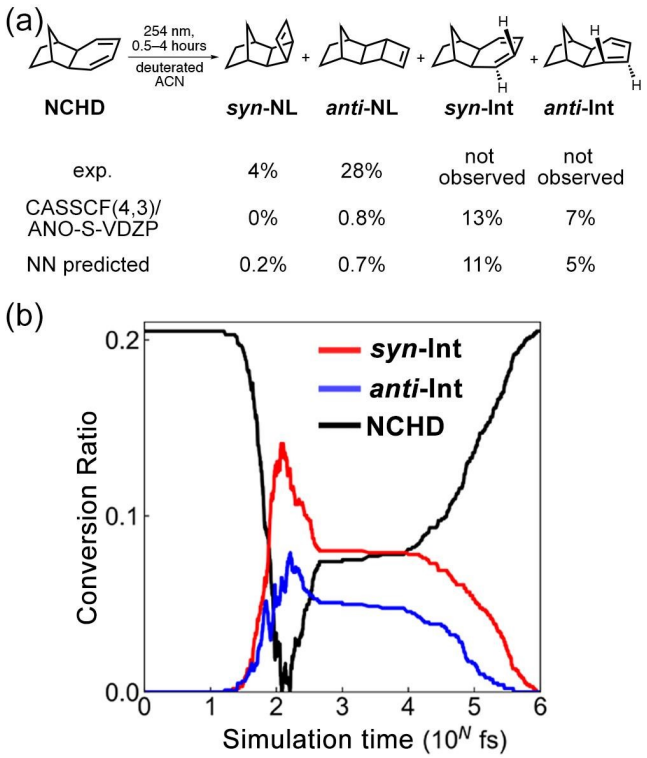

Figure 4. (a) The 4π-electrocyclization of norbornyl cyclohexa-1,3-diene with experimental and predicted reaction yields. The predicted yields are obtained from 1 ps QC and ML-NAMD simulations. (b) Plot for NN predicted photochemical and thermal interconversions between cyclohexa-1,3-diene (NCHD) and the experimentally absent intermediates, *syn*-Int and *anti*-Int in 1 ns. The plot in the first 100 fs shows the photochemical conversion from NCHD to *syn*-Int and *anti*-Int. The following plot shows the thermal conversion from the intermediates back to NCHD. The plot suggests a short thermal lifetime of intermediates of about 1 ns. Results are reproduced from the reference[94] with permission from the Royal Society of Chemistry.

The predicted intermediates in QC NAMD simulations raise a fundamental question on the prediction reliability of the CASSCF(4,3)/ANO-S-VDZP calculations simulating the photochemical reaction of norbornyl cyclohexa-1,3-diene. With ML accelerations, we extended the simulations to 1 ns to monitor the subsequent dynamics of the intermediates. The trajectories showed continued thermal isomerization of the intermediate back to reactant in 1 ns (Figure 4b). This finding confirmed the metastability of the intermediates and explained their absence in the experiments. This example highlighted the advantages of ML photodynamics simulations in studying complex (photo)chemical reaction mechanisms involving elusive and long-lived intermediates.

3.3. Photochemical [2+2] cycloaddition of substituted [3]-ladderdienes

The substituent effects play an essential role in the [2+2]-cycloaddition of [3]-ladderdiene that facilitates the formation of cubane, a class of highly-strained organic molecules. Experiments reported an increasing quantum yield (QY) of cubane following the order of methyl (CH_3), trifluoromethyl (CF_3), and cyclopropyl (cPr) groups in the octa-substituted [3]-ladderdienes (Figure 5a).[74] Uncovering substituent effects has been impossible for decades because octa-substitutions significantly raise the computational cost. For instance, the 1 ps NAMD simulations with CASSCF(8,7)/ANO-S-VDZP+ANO-S-MB(for substituents) calculations for the octamethyl [3]-ladderdiene would take several months. The ML photodynamics simulations can handle full dimensionality greater than 200 degrees of freedom with affordable computational cost. As such, ML photodynamics simulations have been applied to study the substituent effects.[74]

The NN potentials built by the MLP model showed the flexibility of the NN learning various kinds of photochemical reactions. The training data generation solely used the Wigner sampling for the octa-substituted [3]-ladderdiene and the geometrical interpolations from the optimized geometries of octa-substituted [3]-ladderdiene, the S_1/S_0 minimum energy conical intersection (MECI) of the [2+2]-cycloadditions, and the corresponding cubane derivatives. The nuclear displacements of the Wigner sampled geometries were mixed into the interpolated geometries to expand the structural diversity in the training data. Initial training data were 4321 for octamethyl [3]-ladderdiene and 3361 for octatrifluoromethyl and octacyclopropyl [3]-ladderdiene.

The octa-substituted [3]-ladderdienes have a C_2 symmetry in their connection graph. Thus, a permutation map according to the C_2 symmetry was used to automatically expand the training data maintaining the permutational invariance in the total energy and the covariance in the forces.[74] The generated data contains the structural information in the permuationally equivalent geometries following the C_2 relationship without computing more training data or spending more adaptive sampling iterations to search them. Thus, a permutation map helped minimize the requisite training data size and speed up active learning. It leads to a moderate increase of the data size in 1.98–2.23 times when it finds the optimal NN potential with 125 trail trajectories exploring the excited-state PESs (Figure 5c). Thus, it effectively maintains a manageable computational cost of the NN potential training at the CASSCF(8,7)/ANO-S-VDZP+ANO-S-MB(R) level. The final MAE of NN energy predictions were 0.040–0.046, 0.032–0.045, and 0.037–0.039 eV for the octamethyl, octatrifluoromethyl, and octacyclopropyl [3]-ladderdiene, respectively.

The NN potential showed 1.5–6.4·10^4-fold accelerations to the energies and forces computations with the CASSCF(8,7)/ANO-S-VDZP+ANO-S-MB(R) calculations for the substituted [3]-ladderdiene. The ML photodynamics simulations propagated 3835, 3259, and 3122 trajectories from the S_1-FC points in 2 ps with a 0.5 fs time step for the octamethyl, octatrifluoromethy, and octacyclopropyl [3]-ladderdiene. The simulations uncovered four S_1 relaxation pathways of octamethyl [3]-ladderdiene, including the [2+2]-cycloaddition, 4π-disrotatory electrocyclic ring-opening, σ_{C-C} cleavage, and 6π-conrotatory electrocyclic ring-opening (Figure 5b). It showed the 4π and 6π-ring-opening reactions are faster than the [2+2] cycloaddition when R = CH_3. The CF_3 has close-shell repulsion to block the 6π-ring-opening pathway enhancing the preference of the [2+2] cycloaddition. The cPr are steric repulsive, further accelerating the [2+2]-cycloaddition reaction and completing the 4π-ring-opening reaction. The predicted reaction QYs were 1%, 14%, and 15% for the octamethyl, octatrifluoromethy, and octacyclopropyl cubane, in line with the trend observed in the experiment.

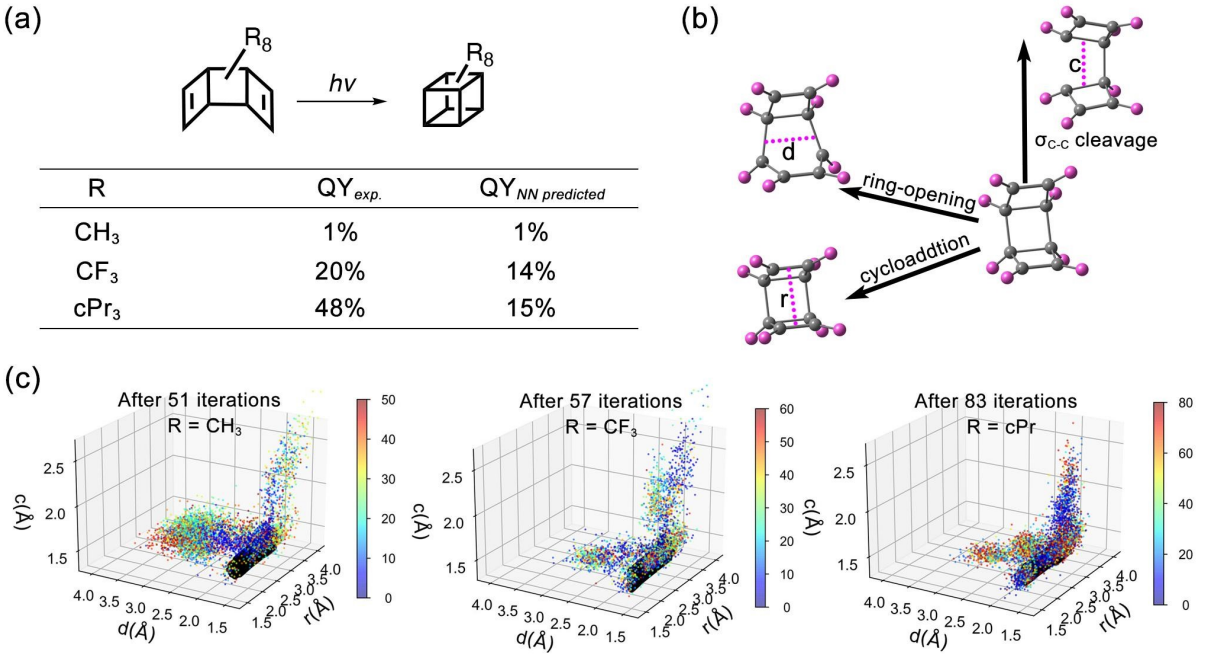

R	$QY_{exp.}$	$QY_{NN\ predicted}$
CH_3	1%	1%
CF_3	20%	14%
cPr_3	48%	15%

Figure 5. (a) Photochemical [2+2] cycloaddition of octa-substituted [3]-ladderdienes toward cubanes with experimental and NN predicted QYs. (b) Three reaction coordinates, *r*, *d*, and *c*, corresponding to the [2 + 2] cycloaddition, electrocyclic ring-opening, and σ_{C-C} cleavage pathways observed in the NN trajectories of octa-substituted [3]-ladderdienes, respectively. (c) Geometrical distributions of the training data for the NN potential of cta-substituted [3]-ladderdienes. The initial set is in black. The color bar of the data shows the interactions of the adaptive sampling. The final training set contains 9303, 6659, and 7697 data points for R = CH_3, CF_3, and cPr. Results are reproduced from the reference[74] with permission. Copyright 2021 American Chemical Society.

3.4. Photochemical 4π-electrocyclization of fluorobenzenes

The nanosecond-scaled NAMD simulations enabled by the ML photodynamics approach provide an effective tool for studying the photochemical reactions involving long-lived photoexcited species. Fluorobenzenes are one example of the excited-state lifetimes falling in nanoseconds' time window (Figure 6a).[75] Moreover, the fluorinations of benzene introduce unusual low-lying πσ* states strongly coupled with the ππ* states. Thus, investigating the excited-state dynamics and subsequent photochemical reactions of fluorobenzenes requires a highly accurate description of the excited-state PES at the XMS-CASPT2 level. However, the NAMD simulations in nanoseconds at the XMS-CASPT2 level are far beyond the affordable computing resources.

The ML photodynamics simulations revealed the photochemical reaction mechanism of fluorobenzenes with high-fidelity structural information. The NN potentials built by the MLP model successfully learned the excited-state properties of the highly symmetric fluorobenzene structures with the help of a permutation map (Figure 6b).[75] The training data were generated using the Wigner sampled structures of fluorobenzenes at their equilibrium geometries and the interpolated structures from the optimized geometries of fluorobenzenes to the corresponding Dewar-fluorobenzenes via an S_1/S_0 MECI. The number of initial training data computed at XMS-CASPT2(6,7)/aug-cc-pVDZ level are 901, 3104, 1677, and 4543 for hexafluorobenzene, pentafluorobenzene, tetrafluorobenzene and trifluorobenzenes. The hexafluorobenzene and tetrafluorobenzene have notably smaller data sizes than the others because they have chemically equivalent reaction channels at symmetric carbon atoms. The adaptive samplings continued to explore the undersampled structures. The S_1 PESs of fluorobenzenes display S_1 minimum regions near the S_1-FC regions, which prevent the trajectories from moving farther in picoseconds. As such, the adaptive sampling scaled the initial kinetic energies 2–3 times to

fast forward the excited-state dynamics fluorobenzenes, so adaptive sampling can be done using 200 trajectories propagated from S_1 in 10 ps. As shown in Figure 6c, using a permutation map notably accelerated the training process for hexafluorobenzene (Figure 6c). With permutations, the completion ratio of adaptive sampling increase to 0.8 in 10 iterations and exceeds 0.9 in 30 iterations; without permutations, the adaptive sampling curve fluctuates in the first 20 iterations, which spent 29 iterations to meet a completion ratio of 0.8. The adaptive sampling with permutations found considerably fewer structures (2128) than that without permutations (3029). At the end of adaptive sampling, the training data size increased to 3051, 4037, 4710, and 10204 for hexafluorobenzene, pentafluorobenzene, tetrafluorobenzene, and trifluorobenzene, respectively. The final MAE of NN energies were accordingly 0.027–0.028, 0.020–0.021, 0.030–0.036, and 0.023–0.024 eV.

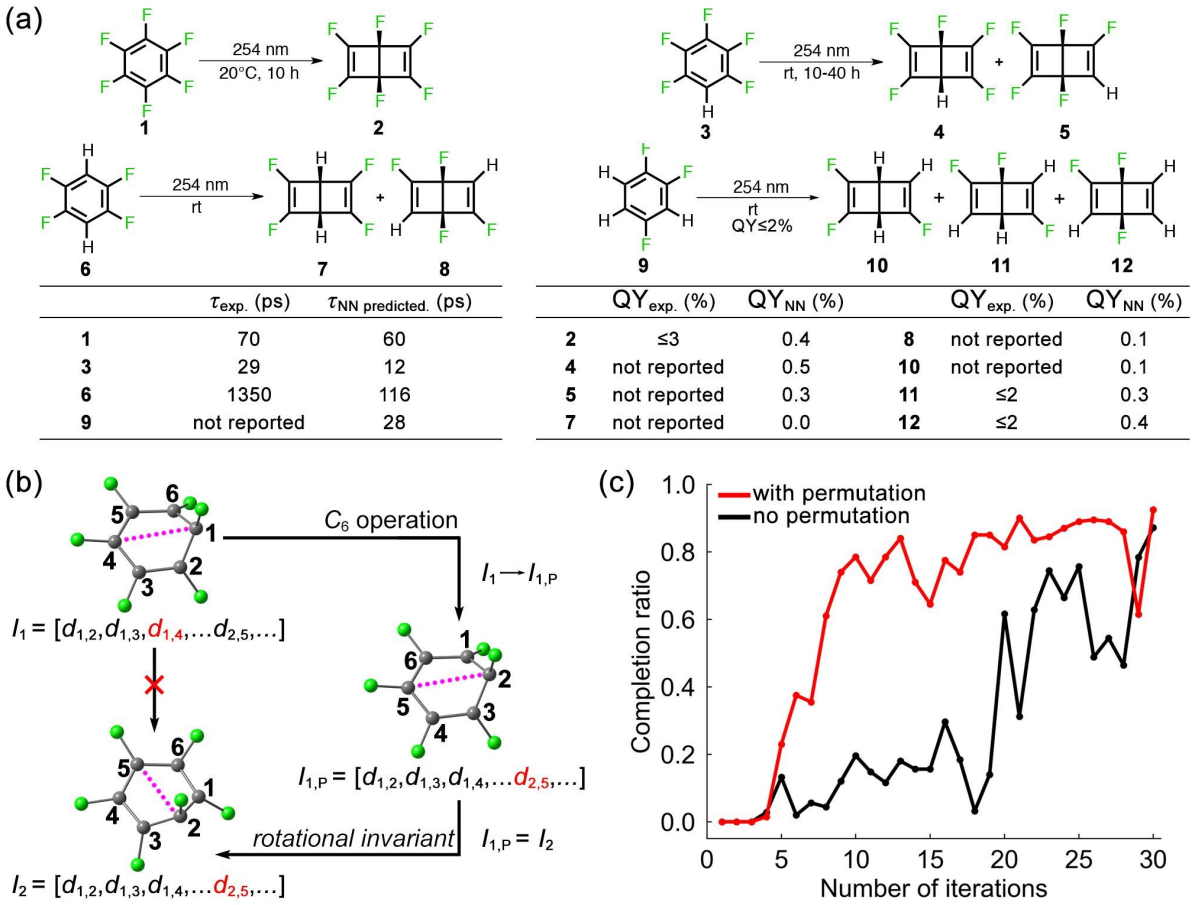

	$\tau_{exp.}$ (ps)	$\tau_{NN\ predicted.}$ (ps)
1	70	60
3	29	12
6	1350	116
9	not reported	28

	$QY_{exp.}$ (%)	QY_{NN} (%)		$QY_{exp.}$ (%)	QY_{NN} (%)
2	≤3	0.4	**8**	not reported	0.1
4	not reported	0.5	**10**	not reported	0.1
5	not reported	0.3	**11**	≤2	0.3
7	not reported	0.0	**12**	≤2	0.4

Figure 6. (a) Photochemical 4π-electrocyclization of fluorobenzenes with reported experimental and NN-predicted excited-state lifetimes and QYs. (b) A permutation map for hexafluorobenzene, defined by the "C_6 operation" reordering the atoms around the C_6 axis of hexafluorobenzene. Two different inverse distance matrix representations, I_1 and I_2, for an equivalent structure can be learned simultaneously after reordering the atoms. (c) Adaptive sampling curves of hexafluorobenzene with and without a permutation map. The completion ratio is the number of complete trajectories divided by the total number of trajectories. Panel (b) and (c) are reproduced from the reference[75] with permission. Copyright 2022 Wiley-VCH.

The ML photodynamics simulations with about 1800 trajectories in 4 ns predicted time constants were 116 ps, 60 ps, 28 ps, and 12 ps for tetrafluorobenzene, hexafluorobenzene, trifluorobenzene, and pentafluorobenzene. These results reproduced the experimentally observed trends in the S_1 decay time constants. The trajectories revealed that the long lifetime of hexafluorobenzene originated from the pseudo-Jahn-Teller effects that create a relatively stable excited-state minimum by breaking the D_{6h} symmetry of the benzene ring. The structural distributions of the S_1/S_0 surface hopping points of fluorobenzenes showed no correlation to

the reaction coordinates along with the 4π-electrocyclic ring-closing pathway. This finding suggests the 4π-electrocyclization of fluorobenzene is controlled by the dynamical effects depending on the instantaneous nuclear momentum facilitating the 1,4-carbon bond formation. As a result, the underlying 4π-electrocyclic ring-closing reaction becomes inefficient with predicted QYs of 0.1–0.5% in Dewar-fluorobenzenes, explaining the experimental QYs about 1%.

3.5. Transferrable ML potentials to predict the *cis-trans* isomerizations of azobenzenes. The ongoing ML model development highly desires a transferable ML potential to predict unseen photochemical reactions. However, an ML potential that fits the excited-state PESs of molecules throughout the chemical space is still unavailable. Because of the intensive nature of excitation energy, the decomposition of excited-state energies into atomistic contributions in different kinds of molecules is questionable. The number of excited states involved in the photochemical reactions is also system and problem-dependent, which further complicated the development of the universal ML model for excited states. Recent work by Marquentand and co-workers has shown the first hint at the transferability of the excited states by training ML potential on two isoelectronic molecules.[47] A later work by Gómez-Bombarelli demonstrated significant progress in developing the transferability of NNs for predicting the *cis-trans* isomerizations of a series of azobenzenes (Figure 7a).[162]

The transferable NNs, called adiabatic artificial NN (DANN), were built upon the PaiNN model (Figure 7b).[163] It used scalar and vectorial features to embed the atomic node and edge information and updated the features through equivariant message-passing layers with the neighboring atoms. The scalar output features are mapped to predict atomic contributions to the adiabatic Hamiltonian matrix elements. The adiabatic Hamiltonian was then diagonalized to predict the total energy of each state. The diabatic Hamiltonian matrix helped NN learn the excited-state energies and forces of azobenzene derivatives. It also produces smooth diabatic couplings between the diabatic states, which were rotated from the diabatic basis to the adiabatic basis to fit the NACs. This strategy avoided the direct fitting of the NACs containing nondifferentiable cusp at the CI regions.

The training data contain the geometries of 8269 azobenzene derivatives, including 164 reported in the literature. The geometries were generated by scanning the central CNNC dihedral angle and the CNN/NNC angles corresponding to the rotation and inversion pathways yielding a total of 567037 geometries. The S_0 and S_1 energies and forces were computed using spin-flip TDDFT calculation at the BHHLYP/6-31G* level.[162] Adaptive sampling was then used to find undersampled geometries and retrain the NNs. As the training data included more equilibrium geometries of azobenzenes derivatives than the near-CI geometries, a sampling procedure based on the structural similarity and the S_0/S_1 energy gap was introduced to balance geometry selection during the adaptive sampling by giving higher sampling probability to underrepresented geometries.

To test the performance of the DANN, the energies, forces, NACs, and QYs of 40 unseen azobenzenes derivatives were predicted against the computed and experimental values. The prediction MAEs were 3.06 and 3.77 kcal·mol^{-1} for the S_0 and S_1 states of the unseen species. It should be noted that the MAE of the S_0-S_1 gap was 1.89 kcal·mol$^{-1,}$ contrasting the accuracy of the semiempirical spin-flip TD-DFTB method.[164] The predictions of S_0 and S_1 force leads to errors of 1.72 and 2.31 kcal·mol^{-1}·Å^{-1} with a nice R^2 correlation coefficient near 1. However, The predictions of NACs gave a poor R^2 value of 0.50. These results suggested the diabatization cannot remove the curl component of the NAC vector, which emphasized the difficulty of predicting NACs. The predicted QYs showed a moderate correlation to the experimental yields. The R^2 value was 0.41, indicating numerical errors in the predicted QYs compared to the mean predictor. The Spearman coefficient ρ was 0.71, which suggests the model predicted the QYs in a correct rank. The computational cost of DANN fitted a scaling of

$N^{0.49}$ for N atoms, whereas the SF-TDDFT calculations scaled with $N^{2.8}$. Thus the DANN accelerated the QC calculation by five to six orders of magnitude.

Given the accelerations and transferability of DANN, ML photodynamics simulations were then used to virtually screen azobenzene derivatives for largely red-shifted absorptions and high transformation ratio $QY_{a\rightarrow b}/QY_{b\rightarrow a}$. The dataset contains 3100 combinatorial azobenzene derivatives generated by the literature-informed substitution patterns.[162] Several hypothetical derivatives were identified to have either the $QY_{cis\rightarrow trans}$, $QY_{trans\rightarrow cis}$, or red-shifted absorption wavelength higher or longer than the average values of the compound space.

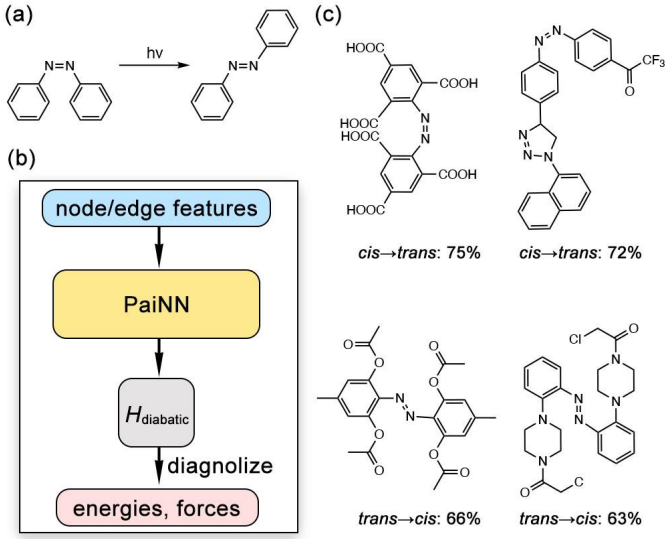

Figure 7. (a) *Cis*-trans isomerization of azobenzene systems. (b) Schematic representation of the DANN model. The atoms and interatomic distances in azobenzenes are embedded into node and edge features and updated by equivariant message-passing layers in PaiNN. The outputs are mapped to the diabatic Hamiltonian matrix elements, which are diagonalized to predict the adiabatic energies and forces. (c) Virtual screening identified azobenzene derivatives with high $QY_{cis\rightarrow trans}$ and $QY_{trans\rightarrow cis}$. The QYs are cited from the reference.[162]

3.6. Roaming mechanism of photoexcited tyrosine

Amino acids feature ultrafast nonradiative decay from the electronically excited state to the ground state. The process is faster than the harmful photochemical reactions, thus, preventing photodamage caused by UV/visible light. Understanding the photochemical reaction mechanism of amino acids can substantially contribute to improving the photostability of peptides and proteins in the design of novel drugs in phototherapy. Tyrosine is one of the amino acids prone to photoexcitation by sunlight. The major deactivation pathway of tyrosine is the photodissociation of the O–H bond located on the phenol ring. Two main dissociation channels in a fast and a slow timescale have been proposed for tyrosine after photoexcitation using 200 nm laser pulses.[165] Experimental studies conducted on tyrosine cannot resolve the O–H bond photodissociation mechanism or trace the roaming atoms. Theoretical studies revealed a repulsive $\pi\sigma^*$ state that can lead to photodissociation,[166] but have been limited to static calculations or low accuracy.[166, 167] More comprehensive computational simulations are needed to uncover the excited-state dynamics of tyrosine, but these remain computationally infeasible.

Marquetand and co-workers applied the SchNarc approach to comprehensively investigate the excited-state dynamics of photoexcited tyrosine. The SchNarc approach performs ML photodynamics simulation using trajectories surface hopping with arbitrary couplings (SHARC)[168] and ML potential built by SchNet models.[53] They trained two NNs to predict the excited-state energies, forces and approximated NACs and a third NN to predict the SOCs. The training data of tyrosine included the energies and forces for 5 singlet states and 8 triplet states and the SOCs between them, which yield 29 energies, 29 forces, and 812 SOCs. Figure

8a illustrates a flowchart of training the SchNarc model. The structures were initially sampled by scanning the normal modes of the 12 lowest energy conformers of tyrosine and the transformation from the neutral to the zwitterionic form, which gave 1967 data points. The training data were mainly computed with ADC(2)/cc-pVDZ calculations because they agreed better with the absorption spectrum of tyrosine than the CASSCF or CASPT2 calculation. These data were used in an initial adaptive sampling running 100 trajectories for each conformer until the number of data points approximately doubled. The initial adaptive sampling explored the PESs in each state without surface hopping between the same spin multiplicity, which collected 16738 data points. However, the ADC(2) method cannot correctly describe the degeneracy between the excited and ground states for the bond-forming and breaking processes. Thus, *ad hoc* data were computed using CASPT2(12, 11)/ANO-RCC-pVDZ calculations when the distance between the hydrogen atom and another atom is longer than empirically defined thresholds. To enable long timescale simulation, another adaptive sampling was used to train the ML potential of tyrosine with 200 trajectories propagated from the S_4 state in 3 ps, finally giving 17265 data points. The MLP models were used to train the ML potential during the adaptive sampling because it is 18 times faster than the SchNet models. The SchNet models were used to learn the final training data and ML photodynamics simulation, as they produced more accurate results and MLP.

About 1000 ML photodynamics trajectories were excited to the S_4 within the excitation window of 6.5–7.0 eV and propagated in 10 ps to inform the photochemistry of tyrosine. 83% of the trajectories showed direct dissociation of a hydrogen atom, the formation of a zwitterionic species, and other fragmentations pathways. 17% of the trajectories found a roaming hydrogen atom after the photodissociation of the O-H bond (Figure 8b). Of these roaming trajectories, 36% stayed with roaming hydrogen atoms, whereas the other trajectories moved toward diverse fragmentation pathways. These results revealed the roaming mechanisms beyond the chemical intuition in peptides and proteins, which brings our knowledge further toward a better understanding of the photostability and photodamage of biological systems.

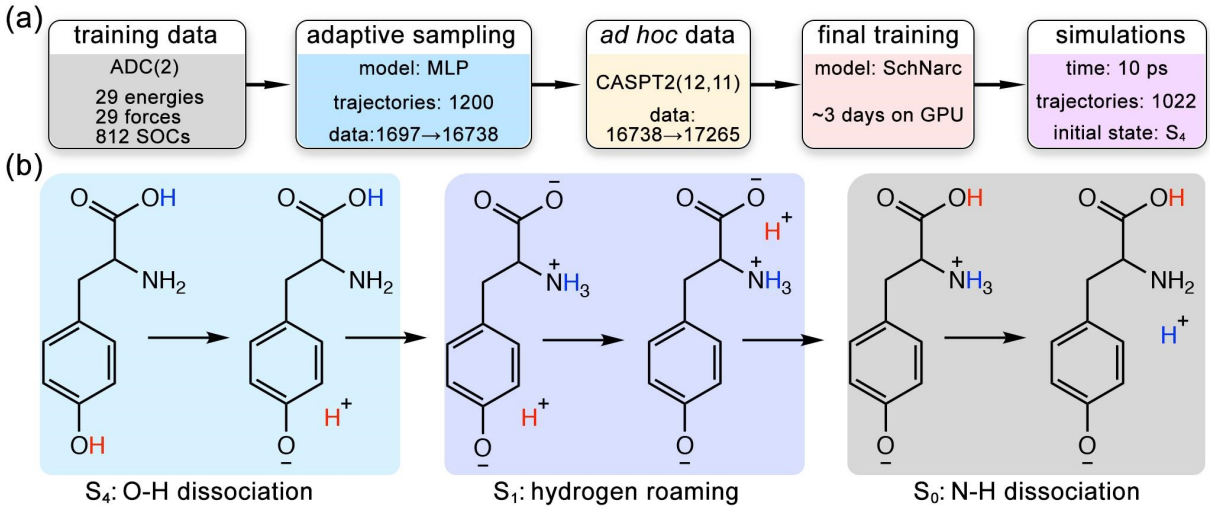

Figure 8. (a) Flowchart for illustration of training SchNarc model. (b) NN revealed the light-induced hydrogen roaming mechanism of tyrosine. The technical information and mechanism were summarized according to the reference.[128]

4. Conclusion

ML photodynamics approach has become an emerging tool for learning photochemistry. The extraordinary accelerations by ML techniques offer great potential for resolving the elusive photochemical reaction mechanisms at an atomistic level in an ultrafast timescale. The recent development of ML models enables accurate predictions of energies and forces of the same quality as quantum chemical calculations. The training protocol with adaptive sampling can

effectively search the undersampled data out of the initial set generated based on chemical intuition, reducing human bias in the training data generation. The reviewed studies have shown ML photodynamics simulations from picoseconds to nanoseconds for various molecules in medium and large sizes. The ML photodynamics simulations provided a high fidelity of trajectories to inform the excited-state structural information underlying the reactivities, stereoselectivity, and unseen mechanistic pathways in complex photochemical reactions.

While the applications of ML photodynamics in photochemistry grow rapidly, several limitations need to be addressed in the ongoing and future method development. First, an accurate ML model for predicting NACs is unavailable. Using the approximated NACs derived from the ML energies, forces, and Hessian does not guarantee accurate surface hopping when the excited and ground state energy gap is significant. The surface hopping calculations depends on the energy gap, which could be smaller than 1 kcal·mol^{-1}. Thus, ML potential needs higher accuracy than the commonly accepted chemical accuracy, at least for structures near the state-crossing regions. The transferability of the ML potential for excited states remains largely unexplored. The few studies describe a transferable ML potential limited to isoelectronic molecules or derivatives undergoing similar mechanistic pathways. Therefore, a universal ML potential for representing the excited states of molecules with arbitrary size and composition is desired for fully exploiting the advantages of ML photodynamics for studying photochemistry.

Acknowledgments
J. L. thanks the supports from the Hoffmann Institute of Advanced Materials at Shenzhen Polytechnic. S.A.L. acknowledges the National Science Foundation CAREER award (NSF-CHE-2144556) and NSF Institute for Data Driven Dynamical Design (NSF-OAC-2118201). All authors appreciate the assistance from the Northeastern Research Computing Team and the computing resources provided by the Massachusetts Life Science Center grant (G00006360).

References
1. de Meijere, A.; Redlich, S.; Frank, D.; Magull, J.; Hofmeister, A.; Menzel, H.; Konig, B.; Svoboda, J. Octacyclopropylcubane and some of its isomers. *Angew Chem Int Ed Engl* **2007**, *46* (24), 4574-4576. DOI: 10.1002/anie.200605150.
2. Poplata, S.; Troster, A.; Zou, Y. Q.; Bach, T. Recent Advances in the Synthesis of Cyclobutanes by Olefin [2+2] Photocycloaddition Reactions. *Chem. Rev.* **2016**, *116* (17), 9748-9815. DOI: 10.1021/acs.chemrev.5b00723.
3. Ma, J.; Chen, S.; Bellotti, P.; Guo, R.; Schafer, F.; Heusler, A.; Zhang, X.; Daniliuc, C.; Brown, M. K.; Houk, K. N.; et al. Photochemical intermolecular dearomative cycloaddition of bicyclic azaarenes with alkenes. *Science* **2021**, *371* (6536), 1338-1345. DOI: 10.1126/science.abg0720.
4. Karkas, M. D.; Porco, J. A., Jr.; Stephenson, C. R. Photochemical Approaches to Complex Chemotypes: Applications in Natural Product Synthesis. *Chem. Rev.* **2016**, *116* (17), 9683-9747. DOI: 10.1021/acs.chemrev.5b00760.
5. Pitre, S. P.; Overman, L. E. Strategic Use of Visible-Light Photoredox Catalysis in Natural Product Synthesis. *Chem. Rev.* **2022**, *122* (2), 1717-1751. DOI: 10.1021/acs.chemrev.1c00247.
6. Gravatt, C. S.; Melecio-Zambrano, L.; Yoon, T. P. Olefin-Supported Cationic Copper Catalysts for Photochemical Synthesis of Structurally Complex Cyclobutanes. *Angew Chem Int Ed Engl* **2021**, *60* (8), 3989-3993. DOI: 10.1002/anie.202013067.
7. Xie, J.; Zhang, X.; Shi, C.; Pan, L.; Hou, F.; Nie, G.; Xie, J.; Liu, Q.; Zou, J.-J. Self-photosensitized [2 + 2] cycloaddition for synthesis of high-energy-density fuels. *Sustainable Energy & Fuels* **2020**, *4* (2), 911-920. DOI: 10.1039/c9se00863b.

8. Liu, Y.; Chen, Y.; Ma, S.; Liu, X.; Zhang, X.; Zou, J.-J.; Pan, L. Synthesis of advanced fuel with density higher than 1 g/mL by photoinduced [2 + 2] cycloaddition of norbornene. *Fuel* **2022**, *318*. DOI: 10.1016/j.fuel.2022.123629.
9. Biegasiewicz, K. F.; Griffiths, J. R.; Savage, G. P.; Tsanaktsidis, J.; Priefer, R. Cubane: 50 years later. *Chem. Rev.* **2015**, *115* (14), 6719-6745. DOI: 10.1021/cr500523x.
10. Dong, L.; Feng, Y.; Wang, L.; Feng, W. Azobenzene-based solar thermal fuels: design, properties, and applications. *Chem Soc Rev* **2018**, *47* (19), 7339-7368. DOI: 10.1039/c8cs00470f.
11. Orrego-Hernandez, J.; Dreos, A.; Moth-Poulsen, K. Engineering of Norbornadiene/Quadricyclane Photoswitches for Molecular Solar Thermal Energy Storage Applications. *Acc Chem Res* **2020**, *53* (8), 1478-1487. DOI: 10.1021/acs.accounts.0c00235.
12. Lennartson, A.; Roffey, A.; Moth-Poulsen, K. Designing photoswitches for molecular solar thermal energy storage. *Tetrahedron Lett.* **2015**, *56* (12), 1457-1465. DOI: 10.1016/j.tetlet.2015.01.187.
13. Wang, Z.; Erhart, P.; Li, T.; Zhang, Z.-Y.; Sampedro, D.; Hu, Z.; Wegner, H. A.; Brummel, O.; Libuda, J.; Nielsen, M. B.; et al. Storing energy with molecular photoisomers. *Joule* **2021**, *5* (12), 3116-3136. DOI: 10.1016/j.joule.2021.11.001.
14. Xu, X.; Wang, G. Molecular Solar Thermal Systems towards Phase Change and Visible Light Photon Energy Storage. *Small* **2022**, *18* (16), e2107473. DOI: 10.1002/smll.202107473.
15. Saydjari, A. K.; Weis, P.; Wu, S. Spanning the Solar Spectrum: Azopolymer Solar Thermal Fuels for Simultaneous UV and Visible Light Storage. *Adv. Energy Mater.* **2017**, *7* (3). DOI: 10.1002/aenm.201601622.
16. Petersen, A. U.; Hofmann, A. I.; Fillols, M.; Manso, M.; Jevric, M.; Wang, Z.; Sumby, C. J.; Muller, C.; Moth-Poulsen, K. Solar Energy Storage by Molecular Norbornadiene-Quadricyclane Photoswitches: Polymer Film Devices. *Adv Sci (Weinh)* **2019**, *6* (12), 1900367. DOI: 10.1002/advs.201900367.
17. Hull, K.; Morstein, J.; Trauner, D. In Vivo Photopharmacology. *Chem. Rev.* **2018**, *118* (21), 10710-10747. DOI: 10.1021/acs.chemrev.8b00037.
18. Cox, B.; Booker-Milburn, K. I.; Elliott, L. D.; Robertson-Ralph, M.; Zdorichenko, V. Escaping from Flatland: [2 + 2] Photocycloaddition; Conformationally Constrained sp(3)-rich Scaffolds for Lead Generation. *ACS Med Chem Lett* **2019**, *10* (11), 1512-1517. DOI: 10.1021/acsmedchemlett.9b00409.
19. Stanley, P. M.; Haimerl, J.; Shustova, N. B.; Fischer, R. A.; Warnan, J. Merging molecular catalysts and metal-organic frameworks for photocatalytic fuel production. *Nat. Chem.* **2022**. DOI: 10.1038/s41557-022-01093-x.
20. Oburn, S. M.; Huss, S.; Cox, J.; Gerthoffer, M. C.; Wu, S.; Biswas, A.; Murphy, M.; Crespi, V. H.; Badding, J. V.; Lopez, S. A.; et al. Photochemically Mediated Polymerization of Molecular Furan and Pyridine: Synthesis of Nanothreads at Reduced Pressures. *J. Am. Chem. Soc.* **2022**, *144* (48), 22026-22034. DOI: 10.1021/jacs.2c09204.
21. Kowalewski, M.; Bennett, K.; Dorfman, K. E.; Mukamel, S. Catching Conical Intersections in the Act: Monitoring Transient Electronic Coherences by Attosecond Stimulated X-Ray Raman Signals. *Phys. Rev. lett.* **2015**, *115* (19), 193003. DOI: 10.1103/PhysRevLett.115.193003.
22. Merritt, I. C. D.; Jacquemin, D.; Vacher, M. Attochemistry: Is Controlling Electrons the Future of Photochemistry? *J. Phys. Chem. Lett.* **2021**, *12* (34), 8404-8415. DOI: 10.1021/acs.jpclett.1c02016.
23. Gruhl, T.; Weinert, T.; Rodrigues, M. J.; Milne, C. J.; Ortolani, G.; Nass, K.; Nango, E.; Sen, S.; Johnson, P. J. M.; Cirelli, C.; et al. Ultrafast structural changes direct the first molecular events of vision. *Nature* **2023**, *615* (7954), 939-944. DOI: 10.1038/s41586-023-05863-6.
24. Zobel, J. P.; González, L. The Quest to Simulate Excited-State Dynamics of Transition Metal Complexes. *JACS Au* **2021**. DOI: 10.1021/jacsau.1c00252.
25. Crespo-Otero, R.; Barbatti, M. Recent Advances and Perspectives on Nonadiabatic Mixed Quantum-Classical Dynamics. *Chem. Rev.* **2018**, *118* (15), 7026-7068. DOI: 10.1021/acs.chemrev.7b00577.

26. Weber, W.; Thiel, W. Orthogonalization corrections for semiempirical methods. *Theoretical Chemistry Accounts: Theory, Computation, and Modeling (Theoretica Chimica Acta)* **2000**, *103* (6), 495-506. DOI: 10.1007/s002149900083.
27. Koslowski, A.; Beck, M. E.; Thiel, W. Implementation of a general multireference configuration interaction procedure with analytic gradients in a semiempirical context using the graphical unitary group approach. *J. Comput. Chem.* **2003**, *24* (6), 714-726. DOI: 10.1002/jcc.10210.
28. Kranz, J. J.; Elstner, M.; Aradi, B.; Frauenheim, T.; Lutsker, V.; Garcia, A. D.; Niehaus, T. A. Time-Dependent Extension of the Long-Range Corrected Density Functional Based Tight-Binding Method. *J. Chem. Theory Comput.* **2017**, *13* (4), 1737-1747. DOI: 10.1021/acs.jctc.6b01243.
29. Zobel, J. P.; Heindl, M.; Plasser, F.; Mai, S.; Gonzalez, L. Surface Hopping Dynamics on Vibronic Coupling Models. *Acc Chem Res* **2021**, *54* (20), 3760-3771. DOI: 10.1021/acs.accounts.1c00485.
30. Plasser, F.; Gomez, S.; Menger, M.; Mai, S.; Gonzalez, L. Highly efficient surface hopping dynamics using a linear vibronic coupling model. *Phys. Chem. Chem. Phys.* **2018**, *21* (1), 57-69. DOI: 10.1039/c8cp05662e.
31. Seritan, S.; Bannwarth, C.; Fales, B. S.; Hohenstein, E. G.; Isborn, C. M.; Kokkila-Schumacher, S. I. L.; Li, X.; Liu, F.; Luehr, N.; Snyder, J. W.; et al. TeraChem: A graphical processing unit-accelerated electronic structure package for large-scale ab initio molecular dynamics. *Wiley Interdiscip. Rev. Comput. Mol. Sci.* **2020**, *11* (2). DOI: 10.1002/wcms.1494.
32. Nandy, A.; Duan, C.; Taylor, M. G.; Liu, F.; Steeves, A. H.; Kulik, H. J. Computational Discovery of Transition-metal Complexes: From High-throughput Screening to Machine Learning. *Chem. Rev.* **2021**, *121* (16), 9927-10000. DOI: 10.1021/acs.chemrev.1c00347.
33. Friederich, P.; Hase, F.; Proppe, J.; Aspuru-Guzik, A. Machine-learned potentials for next-generation matter simulations. *Nat Mater* **2021**, *20* (6), 750-761. DOI: 10.1038/s41563-020-0777-6.
34. Jiang, S.; Malkomes, G.; Moseley, B.; Garnett, R. Efficient nonmyopic active search with applications in drug and materials discovery. *arXiv preprint* **2018**. DOI: 10.48550/arXiv.1811.08871.
35. Jiang, S.; Malkomes, G.; Converse, G.; Shofner, A.; Moseley, B.; Garnett, R. Efficient Nonmyopic Active Search. In Proceedings of the 34th International Conference on Machine Learning, Proceedings of Machine Learning Research; 2017.
36. Lewis-Atwell, T.; Townsend, P. A.; Grayson, M. N. Machine learning activation energies of chemical reactions. *Wiley Interdiscip. Rev. Comput. Mol. Sci.* **2021**. DOI: 10.1002/wcms.1593.
37. Peterson, A. A. Acceleration of saddle-point searches with machine learning. *J. Chem. Phys.* **2016**, *145* (7), 074106. DOI: 10.1063/1.4960708.
38. Pozun, Z. D.; Hansen, K.; Sheppard, D.; Rupp, M.; Muller, K. R.; Henkelman, G. Optimizing transition states via kernel-based machine learning. *J. Chem. Phys.* **2012**, *136* (17), 174101. DOI: 10.1063/1.4707167.
39. Choi, S. Prediction of transition state structures of gas-phase chemical reactions via machine learning. *Nat. Commun.* **2023**, *14* (1), 1168. DOI: 10.1038/s41467-023-36823-3.
40. Hermann, J.; Schatzle, Z.; Noe, F. Deep-neural-network solution of the electronic Schrodinger equation. *Nat. Chem.* **2020**, *12* (10), 891-897. DOI: 10.1038/s41557-020-0544-y.
41. Han, J.; Zhang, L.; E, W. Solving many-electron Schrödinger equation using deep neural networks. *J. Comput. Phys.* **2019**, *399*. DOI: 10.1016/j.jcp.2019.108929.
42. Schutt, K. T.; Gastegger, M.; Tkatchenko, A.; Muller, K. R.; Maurer, R. J. Unifying machine learning and quantum chemistry with a deep neural network for molecular wavefunctions. *Nat. Commun.* **2019**, *10* (1), 5024. DOI: 10.1038/s41467-019-12875-2.
43. Gastegger, M.; McSloy, A.; Luya, M.; Schutt, K. T.; Maurer, R. J. A deep neural network for molecular wave functions in quasi-atomic minimal basis representation. *J. Chem. Phys.* **2020**, *153* (4), 044123. DOI: 10.1063/5.0012911.

44. Zhou, Y.; Wu, J.; Chen, S.; Chen, G. Toward the Exact Exchange-Correlation Potential: A Three-Dimensional Convolutional Neural Network Construct. *J. Phys. Chem. Lett.* **2019**, *10* (22), 7264-7269. DOI: 10.1021/acs.jpclett.9b02838.
45. Dick, S.; Fernandez-Serra, M. Machine learning accurate exchange and correlation functionals of the electronic density. *Nat. Commun.* **2020**, *11* (1), 3509. DOI: 10.1038/s41467-020-17265-7.
46. Gastegger, M.; Behler, J.; Marquetand, P. Machine learning molecular dynamics for the simulation of infrared spectra. *Chem Sci* **2017**, *8* (10), 6924-6935. DOI: 10.1039/c7sc02267k.
47. Westermayr, J.; Marquetand, P. Deep learning for UV absorption spectra with SchNarc: First steps toward transferability in chemical compound space. *J. Chem. Phys.* **2020**, *153* (15), 154112. DOI: 10.1063/5.0021915.
48. Westermayr, J.; Maurer, R. J. Physically inspired deep learning of molecular excitations and photoemission spectra. *Chem Sci* **2021**, *12* (32), 10755-10764. DOI: 10.1039/d1sc01542g.
49. Gao, P.; Zhang, J.; Peng, Q.; Zhang, J.; Glezakou, V. A. General Protocol for the Accurate Prediction of Molecular (13)C/(1)H NMR Chemical Shifts via Machine Learning Augmented DFT. *J. Chem. Inf. Model.* **2020**, *60* (8), 3746-3754. DOI: 10.1021/acs.jcim.0c00388.
50. Westermayr, J.; Marquetand, P. Machine Learning for Electronically Excited States of Molecules. *Chem. Rev.* **2021**, *121* (16), 9873-9926. DOI: 10.1021/acs.chemrev.0c00749.
51. Dral, P. O.; Barbatti, M. Molecular excited states through a machine learning lens. *Nature Reviews Chemistry* **2021**, *5* (6), 388-405. DOI: 10.1038/s41570-021-00278-1.
52. Behler, J. Four Generations of High-Dimensional Neural Network Potentials. *Chem. Rev.* **2021**, *121* (16), 10037-10072. DOI: 10.1021/acs.chemrev.0c00868.
53. Schutt, K. T.; Arbabzadah, F.; Chmiela, S.; Muller, K. R.; Tkatchenko, A. Quantum-chemical insights from deep tensor neural networks. *Nat. Commun.* **2017**, *8*, 13890. DOI: 10.1038/ncomms13890.
54. Unke, O. T.; Meuwly, M. PhysNet: A Neural Network for Predicting Energies, Forces, Dipole Moments, and Partial Charges. *J. Chem. Theory Comput.* **2019**, *15* (6), 3678-3693. DOI: 10.1021/acs.jctc.9b00181.
55. Smith, J. S.; Isayev, O.; Roitberg, A. E. ANI-1: an extensible neural network potential with DFT accuracy at force field computational cost. *Chem Sci* **2017**, *8* (4), 3192-3203. DOI: 10.1039/c6sc05720a.
56. Gao, X.; Ramezanghorbani, F.; Isayev, O.; Smith, J. S.; Roitberg, A. E. TorchANI: A Free and Open Source PyTorch-Based Deep Learning Implementation of the ANI Neural Network Potentials. *J. Chem. Inf. Model.* **2020**, *60* (7), 3408-3415. DOI: 10.1021/acs.jcim.0c00451.
57. Zhang, L.; Han, J.; Wang, H.; Saidi, W. A.; Car, R.; Weinan, E. End-to-end symmetry preserving inter-atomic potential energy model for finite and extended systems. In Proceedings of the 32nd International Conference on Neural Information Processing Systems, Montréal, Canada; 2018.
58. Chmiela, S.; Sauceda, H. E.; Muller, K. R.; Tkatchenko, A. Towards exact molecular dynamics simulations with machine-learned force fields. *Nat. Commun.* **2018**, *9* (1), 3887. DOI: 10.1038/s41467-018-06169-2.
59. Dral, P. O.; Ge, F.; Xue, B. X.; Hou, Y. F.; Pinheiro, M., Jr.; Huang, J.; Barbatti, M. MLatom 2: An Integrative Platform for Atomistic Machine Learning. *Top Curr Chem (Cham)* **2021**, *379* (4), 27. DOI: 10.1007/s41061-021-00339-5.
60. Koner, D.; Meuwly, M. Permutationally Invariant, Reproducing Kernel-Based Potential Energy Surfaces for Polyatomic Molecules: From Formaldehyde to Acetone. *J. Chem. Theory Comput.* **2020**, *16* (9), 5474-5484. DOI: 10.1021/acs.jctc.0c00535.
61. Bartok, A. P.; Payne, M. C.; Kondor, R.; Csanyi, G. Gaussian approximation potentials: the accuracy of quantum mechanics, without the electrons. *Phys. Rev. Lett.* **2010**, *104* (13), 136403. DOI: 10.1103/PhysRevLett.104.136403.

62. Batzner, S.; Musaelian, A.; Sun, L.; Geiger, M.; Mailoa, J. P.; Kornbluth, M.; Molinari, N.; Smidt, T. E.; Kozinsky, B. E(3)-equivariant graph neural networks for data-efficient and accurate interatomic potentials. *Nat. Commun.* **2022**, *13* (1), 2453. DOI: 10.1038/s41467-022-29939-5.
63. Musaelian, A.; Batzner, S.; Johansson, A.; Sun, L.; Owen, C. J.; Kornbluth, M.; Kozinsky, B. Learning local equivariant representations for large-scale atomistic dynamics. *Nat. Commun.* **2023**, *14* (1), 579. DOI: 10.1038/s41467-023-36329-y.
64. Dral, P. O. MLatom: A program package for quantum chemical research assisted by machine learning. *J. Comput. Chem.* **2019**, *40* (26), 2339-2347. DOI: 10.1002/jcc.26004.
65. Xie, Y.; Vandermause, J.; Sun, L.; Cepellotti, A.; Kozinsky, B. Bayesian force fields from active learning for simulation of inter-dimensional transformation of stanene. *npj Computational Materials* **2021**, *7* (1). DOI: 10.1038/s41524-021-00510-y.
66. Westermayr, J.; Faber, F. A.; Christensen, A. S.; von Lilienfeld, O. A.; Marquetand, P. Neural networks and kernel ridge regression for excited states dynamics of CH2NH2+: From single-state to multi-state representations and multi-property machine learning models. *Mach. Learn.: Sci. Technol.* **2020**, *1* (2). DOI: 10.1088/2632-2153/ab88d0.
67. Pinheiro, M., Jr.; Ge, F.; Ferre, N.; Dral, P. O.; Barbatti, M. Choosing the right molecular machine learning potential. *Chem Sci* **2021**, *12* (43), 14396-14413. DOI: 10.1039/d1sc03564a.
68. Rodríguez, L. E. H.; Ullah, A.; Espinosa, K. J. R.; Dral, P. O.; Kananenka, A. A. A comparative study of different machine learning methods for dissipative quantum dynamics. *Mach. Learn.: Sci. Technol.* **2022**, *3* (4). DOI: 10.1088/2632-2153/ac9a9d.
69. Rupp, M.; Tkatchenko, A.; Muller, K. R.; von Lilienfeld, O. A. Fast and accurate modeling of molecular atomization energies with machine learning. *Phys. Rev. lett.* **2012**, *108* (5), 058301. DOI: 10.1103/PhysRevLett.108.058301.
70. Westermayr, J.; Gastegger, M.; Menger, M.; Mai, S.; Gonzalez, L.; Marquetand, P. Machine learning enables long time scale molecular photodynamics simulations. *Chem Sci* **2019**, *10* (35), 8100-8107. DOI: 10.1039/c9sc01742a.
71. Hansen, K.; Biegler, F.; Ramakrishnan, R.; Pronobis, W.; von Lilienfeld, O. A.; Muller, K. R.; Tkatchenko, A. Machine Learning Predictions of Molecular Properties: Accurate Many-Body Potentials and Nonlocality in Chemical Space. *J. Phys. Chem. Lett.* **2015**, *6* (12), 2326-2331. DOI: 10.1021/acs.jpclett.5b00831.
72. Hansen, K.; Montavon, G.; Biegler, F.; Fazli, S.; Rupp, M.; Scheffler, M.; von Lilienfeld, O. A.; Tkatchenko, A.; Muller, K. R. Assessment and Validation of Machine Learning Methods for Predicting Molecular Atomization Energies. *J. Chem. Theory Comput.* **2013**, *9* (8), 3404-3419. DOI: 10.1021/ct400195d.
73. Qu, C.; Yu, Q.; Bowman, J. M. Permutationally Invariant Potential Energy Surfaces. *Annu. Rev. Phys. Chem.* **2018**, *69*, 151-175. DOI: 10.1146/annurev-physchem-050317-021139.
74. Li, J.; Stein, R.; Adrion, D. M.; Lopez, S. A. Machine-Learning Photodynamics Simulations Uncover the Role of Substituent Effects on the Photochemical Formation of Cubanes. *J. Am. Chem. Soc.* **2021**, *143* (48), 20166-20175. DOI: 10.1021/jacs.1c07725.
75. Li, J.; Lopez, S. A. Excited-State Distortions Promote the Photochemical 4pi-Electrocyclizations of Fluorobenzenes via Machine Learning Accelerated Photodynamics Simulations. *Chemistry* **2022**, e202200651. DOI: 10.1002/chem.202200651.
76. Behler, J. Atom-centered symmetry functions for constructing high-dimensional neural network potentials. *J. Chem. Phys.* **2011**, *134* (7), 074106. DOI: 10.1063/1.3553717.
77. Bartók, A. P.; Kondor, R.; Csányi, G. On representing chemical environments. *Phys Rev B Condens Matter* **2013**, *87* (18), 184115. DOI: 10.1103/PhysRevB.87.184115.
78. Christensen, A. S.; Bratholm, L. A.; Faber, F. A.; Anatole von Lilienfeld, O. FCHL revisited: Faster and more accurate quantum machine learning. *J. Chem. Phys.* **2020**, *152* (4), 044107. DOI: 10.1063/1.5126701.
79. Pozdnyakov, S. N.; Willatt, M. J.; Bartok, A. P.; Ortner, C.; Csanyi, G.; Ceriotti, M. Incompleteness of Atomic Structure Representations. *Phys. Rev. Lett.* **2020**, *125* (16), 166001. DOI: 10.1103/PhysRevLett.125.166001.

80. Gilmer, J.; Schoenholz, S. S.; Riley, P. F.; Vinyals, O.; Dahl, G. E. *Arxiv preprint* **2017**. DOI: 10.48550/arXiv.1704.01212.
81. Schutt, K. T.; Sauceda, H. E.; Kindermans, P. J.; Tkatchenko, A.; Muller, K. R. SchNet - A deep learning architecture for molecules and materials. *J. Chem. Phys.* **2018**, *148* (24), 241722. DOI: 10.1063/1.5019779.
82. Lubbers, N.; Smith, J. S.; Barros, K. Hierarchical modeling of molecular energies using a deep neural network. *J. Chem. Phys.* **2018**, *148* (24), 241715. DOI: 10.1063/1.5011181.
83. Unke, O. T.; Chmiela, S.; Gastegger, M.; Schutt, K. T.; Sauceda, H. E.; Muller, K. R. SpookyNet: Learning force fields with electronic degrees of freedom and nonlocal effects. *Nat. Commun.* **2021**, *12* (1), 7273. DOI: 10.1038/s41467-021-27504-0.
84. Tang, D.; Jia, L.; Shen, L.; Fang, W. H. Fewest-Switches Surface Hopping with Long Short-Term Memory Networks. *J. Phys. Chem. Lett.* **2022**, *13* (44), 10377-10387. DOI: 10.1021/acs.jpclett.2c02299.
85. Goodfellow, I.; Bengio, Y.; Courville, A. *Deep Learning*; MIT Press, 2016.
86. Lin, K.; Peng, J.; Gu, F. L.; Lan, Z. Simulation of Open Quantum Dynamics with Bootstrap-Based Long Short-Term Memory Recurrent Neural Network. *J. Phys. Chem. Lett.* **2021**, *12* (41), 10225-10234. DOI: 10.1021/acs.jpclett.1c02672.
87. Mai, S.; Marquetand, P.; González, L. A general method to describe intersystem crossing dynamics in trajectory surface hopping. *Int. J. Quantum Chem.* **2015**, *115* (18), 1215-1231. DOI: 10.1002/qua.24891.
88. Cui, G.; Thiel, W. Generalized trajectory surface-hopping method for internal conversion and intersystem crossing. *J. Chem. Phys.* **2014**, *141* (12), 124101. DOI: 10.1063/1.4894849.
89. Park, W.; Shen, J.; Lee, S.; Piecuch, P.; Filatov, M.; Choi, C. H. Internal Conversion between Bright (1(1)Bu(+)) and Dark (2(1)Ag(-)) States in s-trans-Butadiene and s-trans-Hexatriene. *J. Phys. Chem. Lett.* **2021**, *12* (39), 9720-9729. DOI: 10.1021/acs.jpclett.1c02707.
90. Polyak, I.; Hutton, L.; Crespo-Otero, R.; Barbatti, M.; Knowles, P. J. Ultrafast Photoinduced Dynamics of 1,3-Cyclohexadiene Using XMS-CASPT2 Surface Hopping. *J. Chem. Theory Comput.* **2019**, *15* (7), 3929-3940. DOI: 10.1021/acs.jctc.9b00396.
91. Yang, X.; Manathunga, M.; Gozem, S.; Leonard, J.; Andruniow, T.; Olivucci, M. Quantum-classical simulations of rhodopsin reveal excited-state population splitting and its effects on quantum efficiency. *Nat. Chem.* **2022**, *14* (4), 441-449. DOI: 10.1038/s41557-022-00892-6.
92. Westermayr, J.; Gastegger, M.; Menger, M.; Mai, S.; Gonzalez, L.; Marquetand, P. Machine learning enables long time scale molecular photodynamics simulations. *Chem. Sci.* **2019**, *10* (35), 8100-8107. DOI: 10.1039/c9sc01742a.
93. Westermayr, J.; Gastegger, M.; Marquetand, P. Combining SchNet and SHARC: The SchNarc Machine Learning Approach for Excited-State Dynamics. *J. Phys. Chem. Lett.* **2020**, *11* (10), 3828-3834. DOI: 10.1021/acs.jpclett.0c00527.
94. Li, J.; Reiser, P.; Boswell, B. R.; Eberhard, A.; Burns, N. Z.; Friederich, P.; Lopez, S. A. Automatic discovery of photoisomerization mechanisms with nanosecond machine learning photodynamics simulations. *Chem. Sci.* **2021**, *12* (14), 5302-5314. DOI: 10.1039/d0sc05610c.
95. Axelrod, S.; Shakhnovich, E.; Gómez-Bombarelli, R. Excited state, non-adiabatic dynamics of large photoswitchable molecules using a chemically transferable machine learning potential. *Arxiv preprint* **2021**. DOI: arXiv:2108.04879v2.
96. Ishida, T.; Nanbu, S.; Nakamura, H. Clarification of nonadiabatic chemical dynamics by the Zhu-Nakamura theory of nonadiabatic transition: from tri-atomic systems to reactions in solutions. *Int. Rev. Phys. Chem.* **2017**, *36* (2), 229-285. DOI: 10.1080/0144235x.2017.1293399.
97. Yu, L.; Xu, C.; Lei, Y.; Zhu, C.; Wen, Z. Trajectory-based nonadiabatic molecular dynamics without calculating nonadiabatic coupling in the avoided crossing case: trans<-->cis photoisomerization in azobenzene. *Phys. Chem. Chem. Phys.* **2014**, *16* (47), 25883-25895. DOI: 10.1039/c4cp03498h.

98. Yue, L.; Yu, L.; Xu, C.; Zhu, C.; Liu, Y. Quantum yields of singlet and triplet chemiexcitation of dimethyl 1,2-dioxetane: ab initio nonadiabatic molecular dynamic simulations. *Phys. Chem. Chem. Phys.* **2020**, *22* (20), 11440-11451. DOI: 10.1039/d0cp00811g.
99. Shchepanovska, D.; Shannon, R. J.; Curchod, B. F. E.; Glowacki, D. R. Nonadiabatic Kinetics in the Intermediate Coupling Regime: Comparing Molecular Dynamics to an Energy-Grained Master Equation. *J. Phys. Chem. A* **2021**, *125* (16), 3473-3488. DOI: 10.1021/acs.jpca.1c01260.
100. Yue, L.; Yu, L.; Xu, C.; Lei, Y.; Liu, Y.; Zhu, C. Benchmark Performance of Global Switching versus Local Switching for Trajectory Surface Hopping Molecular Dynamics Simulation: Cis<-->Trans Azobenzene Photoisomerization. *Chemphyschem* **2017**, *18* (10), 1274-1287. DOI: 10.1002/cphc.201700049.
101. T. do Casal, M.; Toldo, J. M.; Pinheiro Jr, M.; Barbatti, M. Fewest switches surface hopping with Baeck-An couplings. *Open Research Europe* **2022**, *1*. DOI: 10.12688/openreseurope.13624.2.
102. Baeck, K. K.; An, H. Practical approximation of the non-adiabatic coupling terms for same-symmetry interstate crossings by using adiabatic potential energies only. *J. Chem. Phys.* **2017**, *146* (6), 064107. DOI: 10.1063/1.4975323.
103. Shu, Y.; Zhang, L.; Chen, X.; Sun, S.; Huang, Y.; Truhlar, D. G. Nonadiabatic Dynamics Algorithms with Only Potential Energies and Gradients: Curvature-Driven Coherent Switching with Decay of Mixing and Curvature-Driven Trajectory Surface Hopping. *J. Chem. Theory Comput.* **2022**, *18* (3), 1320-1328. DOI: 10.1021/acs.jctc.1c01080.
104. Huix-Rotllant, M.; Ferré, N.; Barbatti, M. Time-Dependent Density Functional Theory. In *Quantum Chemistry and Dynamics of Excited States*, 2020; pp 13-46.
105. Christiansen, O.; Koch, H.; Jørgensen, P. The second-order approximate coupled cluster singles and doubles model CC2. *Chem. Phys. Lett.* **1995**, *243* (5-6), 409-418. DOI: 10.1016/0009-2614(95)00841-q.
106. Wormit, M.; Rehn, D. R.; Harbach, P. H. P.; Wenzel, J.; Krauter, C. M.; Epifanovsky, E.; Dreuw, A. Investigating excited electronic states using the algebraic diagrammatic construction (ADC) approach of the polarisation propagator. *Mol. Phys.* **2014**, *112* (5-6), 774-784. DOI: 10.1080/00268976.2013.859313.
107. Dreuw, A.; Wormit, M. The algebraic diagrammatic construction scheme for the polarization propagator for the calculation of excited states. *Wiley Interdiscip. Rev. Comput. Mol. Sci.* **2015**, *5* (1), 82-95. DOI: 10.1002/wcms.1206.
108. Levine, B. G.; Ko, C.; Quenneville, J.; MartÍnez, T. J. Conical intersections and double excitations in time-dependent density functional theory. *Mol. Phys.* **2007**, *104* (5-7), 1039-1051. DOI: 10.1080/00268970500417762.
109. Huix-Rotllant, M.; Nikiforov, A.; Thiel, W.; Filatov, M. Description of Conical Intersections with Density Functional Methods. *Top Curr. Chem.* **2016**, *368*, 445-476. DOI: 10.1007/128_2015_631.
110. Lee, S.; Shostak, S.; Filatov, M.; Choi, C. H. Conical Intersections in Organic Molecules: Benchmarking Mixed-Reference Spin-Flip Time-Dependent DFT (MRSF-TD-DFT) vs Spin-Flip TD-DFT. *J. Phys. Chem. A* **2019**, *123* (30), 6455-6462. DOI: 10.1021/acs.jpca.9b06142.
111. Casanova, D.; Krylov, A. I. Spin-flip methods in quantum chemistry. *Phys. Chem. Chem. Phys.* **2020**, *22* (8), 4326-4342. DOI: 10.1039/c9cp06507e.
112. Horbatenko, Y.; Sadiq, S.; Lee, S.; Filatov, M.; Choi, C. H. Mixed-Reference Spin-Flip Time-Dependent Density Functional Theory (MRSF-TDDFT) as a Simple yet Accurate Method for Diradicals and Diradicaloids. *J. Chem. Theory Comput.* **2021**, *17* (2), 848-859. DOI: 10.1021/acs.jctc.0c01074.
113. Lee, I. S.; Filatov, M.; Min, S. K. Formulation and Implementation of the Spin-Restricted Ensemble-Referenced Kohn-Sham Method in the Context of the Density Functional Tight Binding Approach. *J. Chem. Theory Comput.* **2019**, *15* (5), 3021-3032. DOI: 10.1021/acs.jctc.9b00132.

114. Andersson, K.; Malmqvist, P. A.; Roos, B. O.; Sadlej, A. J.; Wolinski, K. Second-order perturbation theory with a CASSCF reference function. *J. Phys. Chem.* **2002**, *94* (14), 5483-5488. DOI: 10.1021/j100377a012.
115. Andersson, K.; Malmqvist, P. Å.; Roos, B. O. Second-order perturbation theory with a complete active space self-consistent field reference function. *J. Chem. Phys.* **1992**, *96* (2), 1218-1226. DOI: 10.1063/1.462209.
116. Szalay, P. G.; Muller, T.; Gidofalvi, G.; Lischka, H.; Shepard, R. Multiconfiguration self-consistent field and multireference configuration interaction methods and applications. *Chem. Rev.* **2012**, *112* (1), 108-181. DOI: 10.1021/cr200137a.
117. Sherrill, D. C.; Schaefer, H. F. The Configuration Interaction Method: Advances in Highly Correlated Approaches. In *Advances in Quantum Chemistry*, Per-Olov Löwdin, J. R. S., Michael C. Zerner, Erkki Brändas Ed.; Vol. 34; 1999; pp 143-269.
118. Roos, B. O.; Lindh, R.; Malmqvist, P. Å.; Veryazov, V.; Widmark, P.-O. *Multiconfigurational Quantum Chemistry*; 2016.
119. Lischka, H.; Nachtigallova, D.; Aquino, A. J. A.; Szalay, P. G.; Plasser, F.; Machado, F. B. C.; Barbatti, M. Multireference Approaches for Excited States of Molecules. *Chem. Rev.* **2018**, *118* (15), 7293-7361. DOI: 10.1021/acs.chemrev.8b00244.
120. Shiozaki, T.; Gyorffy, W.; Celani, P.; Werner, H. J. Communication: extended multi-state complete active space second-order perturbation theory: energy and nuclear gradients. *J. Chem. Phys.* **2011**, *135* (8), 081106. DOI: 10.1063/1.3633329.
121. Battaglia, S.; Lindh, R. Extended Dynamically Weighted CASPT2: The Best of Two Worlds. *J. Chem. Theory Comput.* **2020**, *16* (3), 1555-1567. DOI: 10.1021/acs.jctc.9b01129.
122. Levine, D. S.; Hait, D.; Tubman, N. M.; Lehtola, S.; Whaley, K. B.; Head-Gordon, M. CASSCF with Extremely Large Active Spaces Using the Adaptive Sampling Configuration Interaction Method. *J. Chem. Theory Comput.* **2020**, *16* (4), 2340-2354. DOI: 10.1021/acs.jctc.9b01255.
123. Park, J. W. Near-Exact CASSCF-Level Geometry Optimization with a Large Active Space using Adaptive Sampling Configuration Interaction Self-Consistent Field Corrected with Second-Order Perturbation Theory (ASCI-SCF-PT2). *J. Chem. Theory Comput.* **2021**, *17* (7), 4092-4104. DOI: 10.1021/acs.jctc.1c00272.
124. Mai, S.; Atkins, A. J.; Plasser, F.; Gonzalez, L. The Influence of the Electronic Structure Method on Intersystem Crossing Dynamics. The Case of Thioformaldehyde. *J. Chem. Theory Comput.* **2019**, *15* (6), 3470-3480. DOI: 10.1021/acs.jctc.9b00282.
125. Gomez, S.; Ibele, L. M.; Gonzalez, L. The 3s Rydberg state as a doorway state in the ultrafast dynamics of 1,1-difluoroethylene. *Phys. Chem. Chem. Phys.* **2019**, *21* (9), 4871-4878. DOI: 10.1039/c8cp07766e.
126. Marin, M. D. C.; Agathangelou, D.; Orozco-Gonzalez, Y.; Valentini, A.; Kato, Y.; Abe-Yoshizumi, R.; Kandori, H.; Choi, A.; Jung, K. H.; Haacke, S.; et al. Fluorescence Enhancement of a Microbial Rhodopsin via Electronic Reprogramming. *J. Am. Chem. Soc.* **2019**, *141* (1), 262-271. DOI: 10.1021/jacs.8b09311.
127. Helmich-Paris, B. Benchmarks for Electronically Excited States with CASSCF Methods. *J. Chem. Theory Comput.* **2019**, *15* (7), 4170-4179. DOI: 10.1021/acs.jctc.9b00325.
128. Westermayr, J.; Gastegger, M.; Voros, D.; Panzenboeck, L.; Joerg, F.; Gonzalez, L.; Marquetand, P. Deep learning study of tyrosine reveals that roaming can lead to photodamage. *Nat. Chem.* **2022**. DOI: 10.1038/s41557-022-00950-z.
129. Kidwell, N. M.; Li, H.; Wang, X.; Bowman, J. M.; Lester, M. I. Unimolecular dissociation dynamics of vibrationally activated CH3CHOO Criegee intermediates to OH radical products. *Nat. Chem.* **2016**, *8* (5), 509-514. DOI: 10.1038/nchem.2488.
130. Rupp, M.; Tkatchenko, A.; Muller, K. R.; von Lilienfeld, O. A. Fast and accurate modeling of molecular atomization energies with machine learning. *Phys. Rev. Lett.* **2012**, *108* (5), 058301. DOI: 10.1103/PhysRevLett.108.058301.
131. Montavon, G.; Rupp, M.; Gobre, V.; Vazquez-Mayagoitia, A.; Hansen, K.; Tkatchenko, A.; Müller, K.-R.; Anatole von Lilienfeld, O. Machine learning of molecular electronic properties

in chemical compound space. *New Journal of Physics* **2013**, *15* (9). DOI: 10.1088/1367-2630/15/9/095003.
132. Ramakrishnan, R.; Hartmann, M.; Tapavicza, E.; von Lilienfeld, O. A. Electronic spectra from TDDFT and machine learning in chemical space. *J. Chem. Phys.* **2015**, *143* (8), 084111. DOI: 10.1063/1.4928757.
133. Ramakrishnan, R.; Dral, P. O.; Rupp, M.; von Lilienfeld, O. A. Quantum chemistry structures and properties of 134 kilo molecules. *Sci Data* **2014**, *1*, 140022. DOI: 10.1038/sdata.2014.22.
134. Chmiela, S.; Tkatchenko, A.; Sauceda, H. E.; Poltavsky, I.; Schutt, K. T.; Muller, K. R. Machine learning of accurate energy-conserving molecular force fields. *Sci Adv* **2017**, *3* (5), e1603015. DOI: 10.1126/sciadv.1603015.
135. Pinheiro, M., Jr.; Zhang, S.; Dral, P. O.; Barbatti, M. WS22 database, Wigner Sampling and geometry interpolation for configurationally diverse molecular datasets. *Sci Data* **2023**, *10* (1), 95. DOI: 10.1038/s41597-023-01998-3.
136. Kästner, J. Umbrella sampling. *Wiley Interdiscip. Rev. Comput. Mol. Sci.* **2011**, *1* (6), 932-942. DOI: 10.1002/wcms.66.
137. Tao, G. Trajectory-guided sampling for molecular dynamics simulation. *Theor. Chem. Acc.* **2019**, *138* (3). DOI: 10.1007/s00214-018-2413-y.
138. Yang, Y. I.; Shao, Q.; Zhang, J.; Yang, L.; Gao, Y. Q. Enhanced sampling in molecular dynamics. *J. Chem. Phys.* **2019**, *151* (7), 070902. DOI: 10.1063/1.5109531.
139. Herr, J. E.; Yao, K.; McIntyre, R.; Toth, D. W.; Parkhill, J. Metadynamics for training neural network model chemistries: A competitive assessment. *J. Chem. Phys.* **2018**, *148* (24), 241710. DOI: 10.1063/1.5020067.
140. Shang, C.; Liu, Z. P. Stochastic Surface Walking Method for Structure Prediction and Pathway Searching. *J. Chem. Theory Comput.* **2013**, *9* (3), 1838-1845. DOI: 10.1021/ct301010b.
141. Dahl, J. P.; Springborg, M. The Morse oscillator in position space, momentum space, and phase space. *J. Chem. Phys.* **1988**, *88* (7), 4535-4547. DOI: 10.1063/1.453761.
142. Smith, J. S.; Isayev, O.; Roitberg, A. E. ANI-1: an extensible neural network potential with DFT accuracy at force field computational cost. *Chem. Sci.* **2017**, *8* (4), 3192-3203. DOI: 10.1039/c6sc05720a.
143. Artrith, N.; Behler, J. High-dimensional neural network potentials for metal surfaces: A prototype study for copper. *Phys Rev B Condens Matter* **2012**, *85* (4). DOI: 10.1103/PhysRevB.85.045439.
144. Chung, L. W.; Sameera, W. M.; Ramozzi, R.; Page, A. J.; Hatanaka, M.; Petrova, G. P.; Harris, T. V.; Li, X.; Ke, Z.; Liu, F.; et al. The ONIOM Method and Its Applications. *Chem. Rev.* **2015**, *115* (12), 5678-5796. DOI: 10.1021/cr5004419.
145. Zhang, Y. J.; Khorshidi, A.; Kastlunger, G.; Peterson, A. A. The potential for machine learning in hybrid QM/MM calculations. *J. Chem. Phys.* **2018**, *148* (24), 241740. DOI: 10.1063/1.5029879.
146. Chen, W. K.; Fang, W. H.; Cui, G. Integrating Machine Learning with the Multilayer Energy-Based Fragment Method for Excited States of Large Systems. *J. Phys. Chem. Lett.* **2019**, *10* (24), 7836-7841. DOI: 10.1021/acs.jpclett.9b03113.
147. Wu, J.; Shen, L.; Yang, W. Internal force corrections with machine learning for quantum mechanics/molecular mechanics simulations. *J. Chem. Phys.* **2017**, *147* (16), 161732. DOI: 10.1063/1.5006882.
148. Shen, L.; Wu, J.; Yang, W. Multiscale Quantum Mechanics/Molecular Mechanics Simulations with Neural Networks. *J. Chem. Theory Comput.* **2016**, *12* (10), 4934-4946. DOI: 10.1021/acs.jctc.6b00663.
149. Boselt, L.; Thurlemann, M.; Riniker, S. Machine Learning in QM/MM Molecular Dynamics Simulations of Condensed-Phase Systems. *J. Chem. Theory Comput.* **2021**, *17* (5), 2641-2658. DOI: 10.1021/acs.jctc.0c01112.
150. Pan, X.; Yang, J.; Van, R.; Epifanovsky, E.; Ho, J.; Huang, J.; Pu, J.; Mei, Y.; Nam, K.; Shao, Y. Machine-Learning-Assisted Free Energy Simulation of Solution-Phase and Enzyme

Reactions. *J. Chem. Theory Comput.* **2021**, *17* (9), 5745-5758. DOI: 10.1021/acs.jctc.1c00565.
151. Shen, L.; Yang, W. Molecular Dynamics Simulations with Quantum Mechanics/Molecular Mechanics and Adaptive Neural Networks. *J. Chem. Theory Comput.* **2018**, *14* (3), 1442-1455. DOI: 10.1021/acs.jctc.7b01195.
152. Gastegger, M.; Schutt, K. T.; Muller, K. R. Machine learning of solvent effects on molecular spectra and reactions. *Chem Sci* **2021**, *12* (34), 11473-11483. DOI: 10.1039/d1sc02742e.
153. Zeng, J.; Giese, T. J.; Ekesan, S.; York, D. M. Development of Range-Corrected Deep Learning Potentials for Fast, Accurate Quantum Mechanical/Molecular Mechanical Simulations of Chemical Reactions in Solution. *J. Chem. Theory Comput.* **2021**, *17* (11), 6993-7009. DOI: 10.1021/acs.jctc.1c00201.
154. Zinovjev, K. Electrostatic Embedding of Machine Learning Potentials. *J. Chem. Theory Comput.* **2023**, *19* (6), 1888-1897. DOI: 10.1021/acs.jctc.2c00914.
155. Zhang, Y.; Hu, C.; Jiang, B. Embedded Atom Neural Network Potentials: Efficient and Accurate Machine Learning with a Physically Inspired Representation. *J. Phys. Chem. Lett.* **2019**, *10* (17), 4962-4967. DOI: 10.1021/acs.jpclett.9b02037.
156. Zhang, Y.; Xia, J.; Jiang, B. Physically Motivated Recursively Embedded Atom Neural Networks: Incorporating Local Completeness and Nonlocality. *Phys. Rev. Lett.* **2021**, *127* (15), 156002. DOI: 10.1103/PhysRevLett.127.156002.
157. Lier, B.; Poliak, P.; Marquetand, P.; Westermayr, J.; Oostenbrink, C. BuRNN: Buffer Region Neural Network Approach for Polarizable-Embedding Neural Network/Molecular Mechanics Simulations. *J. Phys. Chem. Lett.* **2022**, *13* (17), 3812-3818. DOI: 10.1021/acs.jpclett.2c00654.
158. Richings, G. W.; Habershon, S. Predicting Molecular Photochemistry Using Machine-Learning-Enhanced Quantum Dynamics Simulations. *Acc Chem Res* **2022**, *55* (2), 209-220. DOI: 10.1021/acs.accounts.1c00665.
159. Richings, G. W.; Habershon, S. Direct Quantum Dynamics Using Grid-Based Wave Function Propagation and Machine-Learned Potential Energy Surfaces. *J. Chem. Theory Comput.* **2017**, *13* (9), 4012-4024. DOI: 10.1021/acs.jctc.7b00507.
160. Ullah, A.; Dral, P. O. Speeding up quantum dissipative dynamics of open systems with kernel methods. *New Journal of Physics* **2021**, *23* (11). DOI: 10.1088/1367-2630/ac3261.
161. Ullah, A.; Dral, P. O. One-Shot Trajectory Learning of Open Quantum Systems Dynamics. *J. Phys. Chem. Lett.* **2022**, *13* (26), 6037-6041. DOI: 10.1021/acs.jpclett.2c01242.
162. Axelrod, S.; Shakhnovich, E.; Gomez-Bombarelli, R. Excited state non-adiabatic dynamics of large photoswitchable molecules using a chemically transferable machine learning potential. *Nat. Commun.* **2022**, *13* (1), 3440. DOI: 10.1038/s41467-022-30999-w.
163. Schütt, K. T.; Unke, O. T.; Gastegger, M. Equivariant message passing for the prediction of tensorial properties and molecular spectra. *Arxiv preprint* **2021**. DOI: arXiv:2102.03150.
164. Inamori, M.; Yoshikawa, T.; Ikabata, Y.; Nishimura, Y.; Nakai, H. Spin-flip approach within time-dependent density functional tight-binding method: Theory and applications. *J. Comput. Chem.* **2020**, *41* (16), 1538-1548. DOI: 10.1002/jcc.26197.
165. Iqbal, A.; Stavros, V. G. Active Participation of 1πσ* States in the Photodissociation of Tyrosine and Its Subunits. *J. Phys. Chem. Lett.* **2010**, *1* (15), 2274-2278. DOI: 10.1021/jz100814q.
166. Tomasello, G.; Wohlgemuth, M.; Petersen, J.; Mitric, R. Photodynamics of free and solvated tyrosine. *J. Phys. Chem. B* **2012**, *116* (30), 8762-8770. DOI: 10.1021/jp302179m.
167. Sobolewski, A. L.; Shemesh, D.; Domcke, W. Computational studies of the photophysics of neutral and zwitterionic amino acids in an aqueous environment: tyrosine-(H(2)O)(2) and tryptophan-(H(2)O)(2) clusters. *J. Phys. Chem. A* **2009**, *113* (3), 542-550. DOI: 10.1021/jp8091754.
168. Mai, S.; Marquetand, P.; Gonzalez, L. Nonadiabatic dynamics: The SHARC approach. *Wiley Interdiscip Rev Comput Mol Sci* **2018**, *8* (6), e1370. DOI: 10.1002/wcms.1370.

TOC

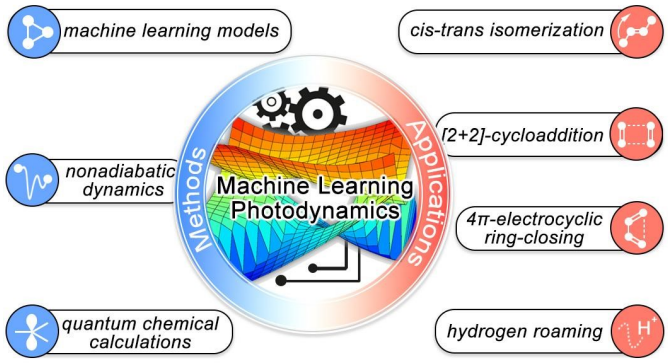
machine learning models
nonadiabatic dynamics
quantum chemical calculations
Methods
Machine Learning Photodynamics
Applications
cis-trans isomerization
[2+2]-cycloaddition
4π-electrocyclic ring-closing
hydrogen roaming
H+